Development of crystallographic preferred orientation during cataclasis in low-temperature carbonate fault gouge

Matteo Demurtas [a,b]*, Steven A. F. Smith [b], David J. Prior [b], Elena Spagnuolo [c], Giulio Di Toro [c,d]

[a] Physics of Geological Processes, The Njord Centre, Department of Geosciences, University of Oslo, Oslo, Norway

[b] Department of Geology, University of Otago, Dunedin 9054, New Zealand

[c] Istituto Nazionale di Geofisica e Vulcanologia (INGV), Rome 00143, Italy

[d] Dipartimento di Geoscienze, Università degli Studi di Padova, 35131 Padova, Italy

* Corresponding author: Matteo Demurtas (matteo.demurtas@geo.uio.no)

Keywords: crystallographic preferred orientation; cataclasis; gouge; granular flow; carbonate; cleavage

Abstract

Grain size reduction due to cataclasis is a key process controlling fault frictional properties during the seismic cycle. We investigated the role of cleavage planes on fracturing and microstructural evolution during cataclasis in wet and dry carbonate fault gouges (50 wt.% calcite, 50 wt.% dolomite) deformed in a rotary-shear apparatus over a wide range of slip rates (30 μms^{-1} to 1 ms^{-1}) and displacements (0.05 to 0.4 m). During shearing, progressive strain localization forms a narrow slip zone that undergoes significant frictional heating (at high slip rates), but the bulk gouge always accommodates low finite shear strains and deforms at low temperatures. Microstructural analysis of the bulk gouges indicates that deformation occurred by brittle fracturing and twinning. Microfractures in calcite are closely spaced, often exploit $\{10\overline{1}4\}$ cleavage *r*-rhomb planes, and occur mainly subparallel to the expected principal stress orientation (σ_1). Instead, twin planes typically occur sub-perpendicular to σ_1. Electron backscatter diffraction analysis of the bulk gouges shows that calcite develops a well-defined crystallographic preferred orientation (CPO) at all investigated deformation conditions. The CPO is defined by a clustering of the calcite c-axes around an orientation sub-parallel to σ_1. The calcite CPO is interpreted to result from grain rotation during granular flow, followed by brittle fracturing that occurred preferentially along calcite cleavage planes. This interpretation is supported by measurements of calcite grain shape-preferred orientations that show a population of elongate calcite grains oriented with their long axes sub-parallel to σ_1. Our experimental results indicate that well-defined CPOs can form at low temperature in cataclastic fault rocks, and that mineral cleavage can strongly influence the evolution of grain sizes and shapes during comminution.

1. Introduction

Gouges and cataclasites are among the most common fault rocks in the upper crust (Snoke et al., 1998). A number of microphysical models have been proposed to describe the grain size evolution (e.g., Allègre et al. 1982, Turcotte, 1986; Sammis et al., 1987; Sammis and King, 2007) and frictional behavior (e.g., Niemeijer and Spiers, 2007; den Hartog and Spiers, 2014; Chen and Spiers, 2016) of gouges and cataclasites. Most of these models assume the deforming grains to have isotropic properties and relatively simple shapes (usually spherical or cylindrical). The development of three-dimensional numerical simulations of gouge evolution has allowed the quantification of force chains (also called grain bridges) during shearing (Hazzard and Mair, 2003; Mair and Hazzard, 2007). These simulations successfully reproduce the complex grain size distributions often found in natural gouges and cataclasites (e.g., Billi et al., 2003; Billi and Storti, 2004; Muto et al., 2015), which are interpreted to result from specific microphysical processes (e.g., constrained comminution; Sammis et al. 1987). An important advance provided by the numerical simulations is the introduction of evolving grain shapes during shearing (Abe and Mair, 2009), which results in modelled friction coefficients consistent with those measured in laboratory experiments.

Natural fault gouges and cataclasites are often composed of minerals that have well-defined cleavage planes, along which fracturing can occur preferentially. The anisotropy represented by cleavage planes is an intrinsic property of carbonates, phyllosilicates, feldspars and amphiboles (e.g., Faulkner et al., 2003; Rutter et al., 2007; Schröckenfuchs et al., 2015; Smeraglia et al., 2016). However, despite the widespread occurrence of these minerals in brittle fault rocks, the influence of cleavage during cataclasis is poorly understood. The aim of this work is to investigate the role of cleavage in the microstructural evolution of fault gouges composed of mixtures of calcite and dolomite. These two minerals were chosen because they have well-developed cleavage planes and are common components of gouges and cataclasites in carbonate-bearing seismogenic fault zones (e.g. Jefferies et al., 2006; Rutter et al., 2007; Demurtas et al., 2016; Delle Piane et al., 2017). To explore a wide range of deformation conditions, rotary-shear experiments were performed on dry and water-dampened gouges composed of calcite and dolomite. Microstructures of the deformed gouges were investigated by electron backscatter diffraction (EBSD) analysis, which facilitates an understanding of possible crystallographic controls on fracturing. The analysis reveals that cleavage plays an important role during fracturing of calcite, and that calcite-bearing gouges can develop well-defined crystallographic preferred orientations (CPOs) during low-temperature brittle deformation, equivalent to conditions experienced during faulting in the uppermost crust. This is significant because CPOs are usually formed by crystal plastic deformation at relatively high homologous temperatures (e.g., Wenk and Christie, 1991; Zhang and Karato, 1995). The recognition and analysis of CPOs that form in natural samples at low temperatures and finite strains will lead to a more complete understanding of deformation in granular materials, and more generally the frictional behavior of upper crustal fault zones.

2. Methods

2.1. Starting materials and rotary-shear experiments

The synthetic gouges were composed of a mixture of 50 wt.% calcite and 50 wt.% dolomite (Fig. 1a). The calcite-dolomite mixtures were obtained by crushing Carrara marble (99.9% calcite) and dolomitized Calcare Massiccio (99% dolomite). The powders were passed through a 250 μm sieve and then mixed together by slow tumbling for c. 30 minutes. In this study, we report microstructural analysis from 19 experiments performed with SHIVA (Slow- to High-Velocity rotary-shear friction Apparatus) installed at the Istituto Nazionale di Geofisica e Vulcanologia in Rome (Table 1; Di Toro et al., 2010; Niemeijer et al., 2011). Gouge layers c. 2.5 mm thick were deformed in a metal sample holder designed for incohesive materials (Fig. 1b; Smith et al., 2013, 2015).

Niemeijer et al. (2011) described the data acquisition systems and the location and calibration of the load cells. Experiments were performed at a constant normal stress of 17.5 MPa over a wide range of deformation conditions: maximum slip rates from 30 μms^{-1} to 1 ms^{-1}, total displacements from 0.05 m to 0.4 m, and in water-dampened and room-humidity conditions (Table 1). Water-dampened experiments were prepared by adding c. 2 ml of distilled water to the top of the gouge layer before the metal sample holder was closed.

2.2. Electron backscatter diffraction analysis

The EBSD analysis was carried out on polished thin sections cut perpendicular to the gouge layer boundaries and parallel to the slip vector (i.e., tangential cuts, inset in Fig. 1c). Data were collected with a Zeiss Sigma VP Field-Emission-Gun Scanning Electron Microscope equipped with a NordlysF EBSD camera from Oxford Instruments at the Otago Centre for Electron Microscopy, University of Otago (New Zealand). Raw diffraction data and energy dispersive spectroscopy (EDS) data were acquired and processed using AZtec software (Oxford Instruments). To overcome the systematic misindexing of calcite and dolomite during data acquisition, the AZtec function *True Phase* was used. *True Phase* uses the EDS spectra to improve phase identification during analysis, in cases where the solutions for the diffraction patterns are not unique (as in the case of calcite and dolomite). The use of combined EDS-EBSD resulted in relatively high indexing rates (up to 70-75%) despite the challenging nature of the samples (i.e., very fine-grained fault gouge with significant porosity). The EBSD data were collected with a 1 μm step size at a working distance between 15 and 19 mm. The instrument was operated at 30 kV accelerating voltage and 60 to 100 nA probe current. Importantly, the EBSD analysis was conducted on the bulk gouges, at distances of > 400-500 μm from the localized principal slip zone that develops during shearing in the high velocity experiments. A schematic representation of the analysis area in the bulk gouge is shown by the orange box in Fig.

1c-d. Previous experiments using the same experimental configuration have shown that the principal slip zone takes up most of the strain during this type of gouge experiment (Smith et al., 2015, 2017; Rempe et al., 2017), and can reach temperatures in excess of those required for decomposition of calcite and dolomite (e.g., Han et al., 2007; De Paola et al., 2015). However, the bulk gouge accommodates relatively low strains (γ < 2-2.5: Smith et al., 2015, 2017; Rempe et al., 2017) and remains at low temperature (< 100 °C) for the duration of the experiments, even at the highest investigated slip velocities (see Section 3.4). Therefore, microstructural analysis of the bulk gouges can be used to understand the evolution of fracturing and cataclasis during the initial stages of granular deformation.

Cleaning and processing of EBSD data were carried out using the MTEX toolbox in MATLAB (Hielscher and Schaeben, 2008). For our samples, a new workflow was created to further improve the identification of calcite and dolomite (Section 1 of Supplementary Material). Dolomite is characterized by systematic misindexing of 180° around the a-axis direction (i.e., $\langle 11\overline{2}0 \rangle$; Section 1 in Supplementary Material; Pearce et al., 2013). Such systematic misindexing is usually overcome by mapping dolomite as Mg-calcite, which has higher crystal symmetry. However, this was not possible in our case due to the presence of both calcite and dolomite in the analyzed material. Although systematic misindexing of dolomite was corrected during data processing, dolomite orientation data had to be interpreted with care. In particular, as a consequence of the systematic misindexing, the polarity of the c-axis was not reliable in dolomite, but the orientation (non-polar) of the c-axis was. To provide further insight in to the textural evolution of calcite and dolomite during shearing, EBSD analysis was performed on experiments consisting of pure calcite (experiment *s269*) and pure dolomite (experiment *s525*). Conditions in these experiments were similar to those imposed during the mixed calcite-dolomite experiments (see Table 1). In the case of the pure dolomite experiment, systematic misindexing was resolved by indexing dolomite as Mg-calcite and thus the c-axis orientation data were reliable.

Grains were reconstructed from processed orientation data following the procedure described by Bachmann et al. (2011). Grain boundaries were defined as having a misorientation angle between neighboring pixels of ≥ 10°. To avoid artefact grains in the analysis, grains that were made of < 10 pixels (i.e., with an equivalent diameter of c. ≤ 3.5 μm) were deleted. Orientation data were plotted both as stereonets and contoured using the Orientation Density Function (ODF, after Bunge, 1982; Bachmann et al., 2010). The ODF was calculated using a de la Vallee Poussin kernel, a half width of 10°, and accounting for one point per grain. All pole figures were plotted as equal area and upper hemisphere.

Fracture and twin orientation analysis was performed on band contrast maps collected during EBSD analysis. Fractures and twin planes were manually identified and their orientations plotted on rose diagrams. Grain shape analysis was performed on SEM backscatter electron images acquired from the same areas as EBSD analysis. Processing of SEM images, grain detection, and measurements were performed in Image SXM (Barrett, 2015).

3. Results

3.1. Mechanical behavior of calcite-dolomite gouges

The mechanical behavior of the calcite-dolomite gouges is consistent with previous studies (e.g., Chen et al., 2013; Rempe et al., 2017; Smith et al. 2017). In room-humidity conditions and slip rates of up to 0.01 ms^{-1}, the gouge mixtures were characterized by an increase of the apparent friction coefficient (μ) with slip (slip strengthening behavior; Fig. 2). The steady-state friction coefficient at these conditions was μ = 0.75-0.80. Decrease of μ with slip (slip-weakening behavior) was initially observed at 0.1 ms^{-1}, while complete dynamic weakening was achieved for slip rates of 1 ms^{-1}, with a steady-state friction coefficient of μ = 0.28 (Fig. 2).

Under water-dampened conditions at slip rates ≤ 0.1 ms^{-1}, the gouges showed a similar frictional evolution consisting of slight slip-strengthening behavior to reach a steady state friction coefficient of μ = 0.62-0.70 (Fig. 2). At higher slip rates (V = 1 ms^{-1}), the evolution of the friction coefficient was similar to the room-humidity experiments. However, the onset of dynamic weakening occurred slightly earlier than in room-humidity conditions (also reported in pure calcite gouges by Rempe et al., 2017).

3.2. Fracture, twin and grain-shape analysis in calcite-dolomite gouges

3.2.1. Fracturing

During sample assembly and prior to shearing, the gouge layers were subjected to 17.5 MPa normal stress (i.e., uniaxial compression). For a sample that experienced only uniaxial compression for 300 seconds (referred to below as uniaxial stress experiment, or *slw* in Table 1), fractures are relatively infrequent and occur in both calcite and dolomite (Fig. 3a and 3f). Fractures are typically oriented sub-parallel to the applied stress orientation (i.e., subvertical in Fig. 3a and 3f). In the deformed gouges, the density of fractures increases significantly (compare Fig. 3f with 3g). Fractures are more abundant in calcite and are preferentially orientated (Fig. 3b-e and 3g). The most prominent set of fractures is orientated 130-140° counterclockwise from the gouge layer boundaries, approximately parallel to the predicted principal stress orientation (σ_1) during simple shear, with a second prominent fracture set orientated at large angles to the gouge layer boundaries (Fig. 3b-e and 3g). SEM and EBSD observations show that the fractures at 130-140° commonly exploit the $\{10\bar{1}4\}$ rhombohedral (*r*) cleavage planes in calcite to form highly fractured aggregates of calcite containing elongate, beam-like fragments (Figs. 3g, 4, 5). In particular, detailed analysis of one highly fractured calcite grain (Fig. 5) shows that the orientation of at least one of the three $\{10\bar{1}4\}$ planes within calcite appears to be sub-parallel to the trace of the fractures for that grain (see the pole figure for $\{10\bar{1}4\}$ in Fig. 5c).

3.2.2. Twinning

Under uniaxial stress conditions, twinning in calcite was uncommon and the overall twin density was in the range of 45 ± 23 mm^{-1} (the number of twin lamellae of a given twin set with respect to the grain diameter measured normal to the trace of the twin lamellae; Rowe and Rutter, 1990). Calcite twins show a large spread in orientations (Fig. 3a), probably reflecting twinning within a gouge layer with an initial uniform CPO (see three pole figures at the top of Fig. 6a). Twinned grains typically contain a single set of relatively straight twins that can be defined as type II (twins 1-5 µm thick) or type I twins (≤ 1 µm thick; Burkhard, 1993).

In deformed gouges, twin planes in calcite were preferentially orientated c. 30-50° counterclockwise to the gouge layer boundaries (Fig. 3b-e). This orientation is sub-perpendicular to the main fracture set and the predicted orientation of σ_1 during shearing. Twins were mostly type II and had planar boundaries (Fig. 3i). In sheared samples the twin density was higher than in the uniaxial experiment (60-78 mm^{-1}; Rowe and Rutter, 1990).

3.2.3. Grain shape analysis

After application of uniaxial stress, calcite grains with an aspect ratio ≥ 1.5 show a shape preferred orientation (SPO) consisting of a population of grains oriented with their long axes around c. 90°-110° counterclockwise from the gouge layer boundaries, sub-parallel to the applied normal load (Fig. 4a). In sheared gouges, calcite grains with aspect ratio ≥ 1.5 developed a SPO composed of two main sets: one set consisting of grains oriented c. 30°±10° counterclockwise from the gouge layer boundaries, and a second set c. 150°±10° counterclockwise from the gouge layer boundaries (Fig. 4b). The latter set is sub-parallel to i) the predicted principal stress during shearing, ii) one of the main fracture sets (Fig. 3b-e) and also iii) the cluster of calcite c-axes that contribute to the CPO described below (see Section 3.3.2 and Fig. 4b).

3.3. Crystallographic preferred orientation (CPO) in calcite and dolomite gouges

3.3.1. CPO in uniaxial stress conditions

As a reference material for the sheared gouges, we measured the CPO of the water-dampened uniaxial stress experiment (experiment *slw* in Table 1 and the three pole figures at the top of Fig. 6a). Both calcite and dolomite grains in the reference material show no CPO (Fig. 6a). Misorientation analysis of the uniaxial stress experiment for random-pair grains (Wheeler et al., 2001) shows a misorientation angle distribution similar to the random misorientation distribution (Fig. 6b; Mackenzie and Thompson, 1957). For neighbor-pair grains, deviations from the expected misorientation angle distribution for a uniform distribution are observed at all the misorientation intervals, with a clear peak at c. 77° (i.e., development of *e*-twins in calcite; Fig. 6b).

3.3.2. CPO in sheared gouges

At all investigated conditions, calcite grains show a CPO characterized by a prominent cluster of the c-axes (i.e., $[0001]$) inclined c. 130-140° counterclockwise to the gouge layer boundaries (which are parallel to the XZ plane in Fig. 6a). This cluster of c-axes is sub-parallel to the expected σ_1 orientation during simple shear (reference diagram in Fig. 6a). The a-axis directions (i.e., $\langle 11\bar{2}0 \rangle$) lie in a girdle sub-perpendicular to the c-axes (Fig. 6a). Calcite CPOs under room-humidity conditions are stronger (max m.u.d. range 1.8-3.4) than those developed in water-dampened experiments (max m.u.d. range 1.4-2.1; see also Section 2 of Supplementary Material for the eigenvalue analysis). One sample showed the development of a well-defined gouge foliation (Fig. 3h) defined mainly by compositional banding of calcite and dolomite in the bulk gouge (i.e., experiment *s1221* in Table 1; also see Smith et al. 2017). In this experiment, the (0001) cluster and the plane containing $[\bar{1}\bar{1}20]$ were oriented, respectively, at a large angle and sub-parallel to the trace of the foliation surfaces.

In both water-dampened and room-humidity conditions, dolomite grains developed CPOs (max m.u.d. range 1.5-2.4) in which the c-axes create one or more clusters with different orientations. Only in experiment *s1221* (V = 1 ms^{-1}, displacement = 40 cm, room-humidity conditions) the dolomite c-axis CPO is similar to the calcite c-axis CPO (Fig. 6a).

The EBSD analysis conducted on pure calcite gouges (experiment *s269* in Table 1) sheared at room-humidity (V = 1.13 ms^{-1} and normal stress = 8.5 MPa) showed the development of a CPO similar to that observed in the calcite-dolomite mixtures (Fig. 6a). In pure dolomite gouges (experiment *s525* in Table 1), EBSD data show multiple clustering of both the c- and a-axes, similar to that of the calcite-dolomite mixtures (Fig. 6a).

Experiments *s1327*, *s1329*, *s1328* and *s1214* were performed under identical deformation conditions (i.e., slip rate of 30 μms^{-1}, constant normal load of 17.5 MPa, water-dampened conditions), but with increasing displacements from 0.05 m (*s1327*) to 0.4 m (*s1214*; Fig. 7). The EBSD analysis of the bulk gouge recovered from these experiments showed no significant variation in the shape of the calcite CPO, but an increase in the strength of the CPO between 0.05 m and 0.1 m (from m.u.d. values of 1.5 at 0.05 m to m.u.d. of 2 at 0.1 m; Fig. 7), after which the strength remained constant.

Misorientation angle distribution analysis of the sheared gouges showed deviations for neighbor- and random-pair grains from the distribution expected for a uniform CPO (Fig. 6c-d). For neighbor-pair grains, besides the clear peak at c. 77° associated with the development of *e*-twins in calcite, a net increase in the frequency is observed between 20° and 35° and a net decrease at high angles (> 80°) (Fig. 6c-d). For experiment *s1214* (V = 30 μms^{-1}, displacement = 40 cm, water-dampened conditions), the random-pair grains misorientation angle distribution reflects that expected for uniformly oriented calcite grains (Fig. 6c). Conversely, for fast slip under room-humidity conditions (experiment *s1221*, V = 1 ms^{-1}, displacement = 40 cm) the random-pair grains misorientation angle distribution differs significantly from the uniform distribution (Fig. 6d), reflecting the development of a clear CPO in calcite (Fig. 6a).

Finally, Figure 8 shows the grain distribution and the resulting CPO for experiment *s1217* only considering near-equant calcite grains (i.e., those characterized by an aspect ratio < 1.5). The grains are evenly distributed within the bulk gouge and range in size from c. 5 μm up to c. 100 μm (see Section 3 of Supplementary Material for additional examples). The CPO is consistent with that measured for the entire population (i.e., including grains with aspect ratio > 1.5) of calcite grains from the same experiment (compare pole figure for experiment slid at 0.01 ms^{-1} in room-humidity conditions in Fig. 6a with Fig. 8), with m.u.d. values indicating a stronger CPO in the case of equant grains (m.u.d. of 2.7 for equant grains in Fig. 8 vs. m.u.d. of 1.8 for all calcite grains in Fig. 6a).

3.4. Temperature measurements and thermal modeling

Temperature variations during deformation in the gouge were measured at an acquisition rate of 2.5 Hz using four K-type thermocouples (Nickel-Alumel) installed on the stationary side of the gouge holder. In particular, one thermocouple was positioned at a distance of c. 200 μm from one of the gouge layer boundaries (Fig. 1b), while the other three thermocouples were located on the sample holder and on the stationary column to detect temperature variations due to heat conduction in the sample assembly. The temperature measurements from the thermocouple nearest to the gouge layer for all the experiments are reported in Fig. 9. The highest temperature

(c. 620 °C) was measured in experiment *s1221* performed under room-humidity conditions at a target V = 1 ms^{-1}. In experiment *s1222* performed at the same experimental conditions (slip rate, normal stress, etc.), but in the presence of liquid water, the maximum temperature was 210 °C (Fig. 9b). For experiments with slip rates ≤ 0.001 ms^{-1}, no significant temperature increases were measured.

Thermal modeling was performed to estimate the temperature rise in the bulk gouge as a result of heat diffusing (i.e., $\frac{dT}{dt} = \kappa\nabla^2 T$; Fourier, 1822) away from the principal slip zone. Thermal modelling was done using the Crank and Nicholson (1947) finite difference method as discussed in Philpotts (1990) and following the methodology presented in Di Toro and Pennacchioni (2004). The model assumed a thermal diffusivity of $1.74*10^{-6}$ m^2s^{-1} for the gouge layers and $4*10^{-6}$ m^2s^{-1} for the sample holder (Aretusini, 2018). The ambient temperature of the bulk gouge and the sample holder was 20 °C (room temperature).

The model is likely to provide an upper bound on the temperature profile present in the gouge layers for the following reasons:

1. Modelling was performed for experiment *s1221* where the highest temperatures (620 °C) were measured with the thermocouple closest to the gouge layers. Other experiments showed significantly lower maximum temperatures (Fig. 9c).
2. The gouge was assumed to be made of pure calcite with no porosity. The presence of pores in the gouge would significantly decrease the thermal diffusivity.
3. The principal slip zone was assumed to be 160 μm thick, whereas microstructural evidence suggests that at high slip rates it is probably < 50 μm thick. This means that in our thermal model the heat generated was approximately three times the expected heat.

The evolution of the modeled temperatures in experiment *s1221* is shown in Fig. 10a. The model shows the temperature profile due to heat diffusion away from a principal slip zone with an initial temperature of 620 °C at t = 0 s (this instant corresponds to the end of the slip pulse, which lasts c. 0.45 s). In the bulk gouge where CPO was measured, the maximum temperature is not predicted to exceed c. 100 °C at 0.5 mm from the PSZ, and c. 50 °C at 1 mm from the PSZ. In other experiments performed at lower target velocities, or in fluid-bearing conditions, the temperatures at any given time are expected to be much lower.

To better investigate the thermal history of the gouge in the first 4-5 cm of slip (hence in the moment during which the CPO is developing) during shearing at 1 ms^{-1}, an additional thermal model was produced (Fig. 10b), assuming that the temperature in the principal slip zone reached 620 °C at the onset of slip (i.e., earlier than it would have in the experiments). This new thermal model reproduces the maximum possible temperatures achieved in the gouge layer, which must be higher than those actually achieved in the experimental slip zone. All the parameters are the same as in the previous thermal model, but the principal slip zone was “heated” at 620 °C for a duration of 0.05 seconds (roughly corresponding to 4-5 cm of slip). According to the model results, at 0.5 mm from the principal slip zone, during the 0.05 s of heating, the gouge reaches a maximum temperature of c. 200 °C. During the same time window, at 1 mm from the principal slip zone, the gouge reaches only ~40 °C (temperature rise of 20 °C from room temperature).

The thermal model presented in Fig. 10b overestimates heat generation significantly, since it is unlikely that the gouge experienced the maximum temperature of 620 °C from the onset of slip. The model provides robust support for a short-lived temperature increase of < 25-200 °C during CPO development in the gouge layer at a distance of 0.5-2.5 mm from the principal slip zone, at an imposed slip rate of 1 ms^{-1} (i.e., the highest slip rate imposed in the experiments). At lower slip rates the temperature increase is negligible in all cases.

4. Discussion

4.1. Mechanisms of CPO and SPO development in granular materials

Crystallographic preferred orientations (CPOs) are most commonly used to constrain deformation and recrystallization processes in mylonites (e.g., Law et al., 1986; Wenk and Christie, 1991; Zhang and Karato, 1995; Prior et al., 1999; Passchier and Trouw, 2005). The development of CPOs in mylonitic shear zones typically occurs at relatively high homologous temperatures, and as such the investigation of CPOs (and associated seismic anisotropy) has been used to decipher the rheological, thermal, and kinematic history of rocks deformed at mid- to lower-crustal depths and in the mantle (e.g., Wenk and Christie, 1991; Zhang and Karato, 1995; Hansen et al., 2011). However, a number of possible CPO-forming mechanisms that do not require dislocation activity have been described, including oriented crystal growth during vein precipitation or diffusion creep in (ultra)mylonites (e.g., Berger and Stünitz, 1996; Bons and Bons, 2003; Okamoto and Sekine, 2011; Getsinger and Hirth, 2014; Giuntoli et al., 2018), crystallographically-controlled mineral dissolution and precipitation combined with rigid body grain rotation during pressure solution (e.g., Power and Tullis, 1989; Bons and den Brok, 2000), and surface energy interactions during grain annealing (e.g., Spiess et al., 2001; Toy et al., 2015).

Recently, CPOs have been reported from the fine-grained slip zones of calcite-dominated faults exhumed from shallow (< 2 km) crustal depths (e.g., Smith et al., 2011; 2013; Bauer et al., 2018). Additionally, CPOs have been documented within localized slip zones and shear bands that formed in carbonates deformed experimentally at sub-seismic (Verberne et al., 2013; Delle Piane et al., 2018) to seismic slip rates (e.g., Smith et al., 2013; Ree et al. 2014; Pozzi et al., 2019). In calcite gouges sheared at seismic slip rates (V = 1.13 ms^{-1}), an intense CPO and mylonitic microstructure was found within c. 300 μm of the experimental slip surface, with the calcite c-axes clustered at large angles to the slip surface (Smith et al., 2013). The CPO was associated with a well-defined shape-preferred orientation (SPO) of elongate calcite grains up to 50 µm long, which were interpreted to have formed by dynamic recrystallization. The development of a CPO was also observed in calcite gouges sheared at sub-seismic velocities (V = 0.1 – 10 μms^{-1}; Verberne et al., 2013; Delle Piane et al., 2018), although the size of the grains (~5-20 nm) contributing to the CPO was much smaller than in the high-velocity experiments of Smith et al. (2013). Verberne et al. (2013) reported extreme comminution (grain size ~5-20 nm) localized along Riedel and boundary shear bands, which they suggested could have promoted deformation of calcite nanograins by dislocation glide along the $\{10\bar{1}4\}$ rhomb *r*-planes at the ambient experimental temperature of 80 °C. They suggested that the activation of dislocation glide in the shear bands, along with cataclasis in the bulk gouge, was responsible for the observed transition from stable velocity strengthening to unstable velocity weakening at T ≥ 80 °C (Verberne et al., 2013).

In the present study, EBSD analysis was focused on the bulk calcite-dolomite gouges (Fig. 1c) that accommodated relatively low finite shear strains (γ < 2-2.5) at distances of > 400-500 µm from the localized slip surfaces that developed during shearing (Smith et al., 2015; Rempe et al., 2017) (Fig. 1c-d). Given the short duration of the experiments during high-velocity slip (< 0.5 s for V = 1 ms^{-1}), and the distance from the slip surface of the analyzed areas, the maximum temperature in the analyzed areas for the high-velocity experiments is expected to be < 50 °C (Fig. 10a), although locally along the slip surfaces and within the principal slip zone, the temperature was high enough for dolomite decarbonation (i.e., > 550 °C, Samtani et al., 2002). For experiments performed at low- to intermediate slip rates (V ≤ 0.01 ms^{-1}), the temperature increase in the principal slip zone was limited to a few tens of degrees, and the temperature increase in the bulk gouges was negligible (Fig. 9c). This is consistent with microstructural observations suggesting that during deformation under all investigated conditions, the bulk gouges remained brittle, with no evidence for recrystallization, porosity reduction by grain growth, or thermal decomposition (Figs. 3g-i and 11). Despite this, our EBSD analysis shows that a well-defined CPO developed in the bulk gouges at all tested conditions, with the c-axes of the calcite grains preferentially oriented sub-parallel to σ_1 (Figs. 6a, 12). The CPO was weaker in water-dampened experiments (Fig. 6a). The relatively high frequency of misorientation angles between 20° and 35° for neighbor-pair grains in the sheared gouges (Fig. 6c-d) is interpreted as due to intragranular fracturing followed by slight rotation of the fractured grains. As a consequence, such grains would be recognized as fracture-bound grains during EBSD analysis (Section 4 in Supplementary Material). No clear evidence for dislocation glide or creep was observed in the bulk gouges. Instead, only twinning and brittle fracturing were identified as important deformation processes in the bulk gouges in our experiments, with many fracture traces being sub-parallel to the c-axis orientations, the $\{10\bar{1}4\}$ cleavage planes, and the predicted principal stress orientation (Figs. 3b-e, 12).

The formation of a CPO in the experiments with 0.05, 0.1 and 0.2 m of slip (Fig.7), as well as in all of the experiments with 0.4 m of slip (Fig. 6a), suggests that the CPO forms during the early stages of shearing, when strain and thus cataclasis are uniformly distributed across the full thickness of the gouge layer (Fig. 1c-d). The CPO in our experiments becomes stronger up to 0.1 m of slip, after which the strength remains approximately the same (Fig. 7). These results are consistent with the quantitative strain measurements made in similar gouge experiments by Smith et al. (2015) and Rempe et al. (2017). These authors showed that at slip rates of 1 ms^{-1} and for an initial layer thickness of 3 mm, the bulk gouge layer is actively shearing for up to 0.1 m of displacement, after which strain becomes progressively localized to a discrete principal slip zone (e.g., Fig. 1c) that accommodates most subsequent displacement. This also helps to explain why the CPO in our experiments is well preserved even after 0.4 m of slip: the bulk gouge is abandoned as strain becomes localized, and thus the early-formed microstructures and textures within the bulk gouge are not reworked during the latter stages of shearing.

We interpret the development of a calcite CPO in the bulk gouges to result from mechanical grain rotation and fracturing of calcite mainly along the $\{10\bar{1}4\}$ cleavage planes (Figs. 3g, 5, 12). After the application of uniaxial stress, the calcite grains in the matrix have a uniform CPO (Fig. 12a). Here, fracturing in the larger clasts occurs mainly sub-parallel to the direction of the applied uniaxial stress, and calcite twins are infrequent (Figs. 3a, 12a). Shape analysis of grains with an aspect ratio ≥ 1.5 highlights a population of grains with their long axes sub-parallel to the uniaxial stress (Fig. 4a). During uniaxial compaction, grain rotation is assumed to be limited and thus no significant change in the calcite grain shapes and CPO is expected.

As shearing initiates in the gouge layers, some calcite grains will rotate until their c-axes lie sub-parallel to the principal stress (Fig. 12b). At this stage, grains in such an orientation will fracture relatively easily along $\{10\bar{1}4\}$ planes (i.e., the *r*-rhomb planes; Fig. 5), which in calcite are orientated at c. 45° to the c-axis. Analysis of grain shapes suggests that this process forms a SPO, with grains (aspect ratio ≥ 1.5) orientated with their long axes either sub-parallel (grain population at c. 150° in Fig. 4b) or at large angles (grain population at c. 30° in Fig. 4b) to σ_1 (and the mode of the CPO). The population at c. 150° is interpreted to form as the fracturing process exploits cleavage planes to produce elongate beams of calcite (Fig. 12b). Instead, the population at c. 30° is interpreted to form as some elongate fragments rotate in to a more stable orientation during granular flow (Cladouhos, 1999). Our observations may represent a snapshot of the early, low-strain stages in the development of "brittle" CPO and SPO in cleaved minerals like calcite. Higher strains and multiple slip events in natural fault gouges may result in more distributed grain comminution and rotation, leading to the destruction of any early-formed CPO and SPO.

The weaker CPO observed in water-dampened experiments (Fig. 6a) could be explained in a number of ways. One possibility is that stress corrosion is more efficient in wet calcite by a factor of three, which can lead to faster crack propagation (Røyne et al., 2011). This effect may result in fracturing of calcite grains before they rotate in to an orientation where the c-axis and $\{10\overline{1}4\}$ *r*-cleavage planes are sub-parallel to the principal stress. Alternatively, wet calcite typically localizes and (at high-velocities) weakens much faster than dry calcite (Violay et al., 2014; Rempe et al., 2017). In wet gouges, this implies that less strain is accommodated in the bulk gouge prior to the onset of dynamic weakening, meaning that fewer calcite grains will rotate in an orientation favorable for fracturing.

The stronger CPO in calcite compared to dolomite could be explained by a lower fracture energy required for crack propagation in calcite. This results in more pervasive fracturing within calcite grains (Figs. 3g and 4b), resulting in rapid grain size reduction in calcite compared to dolomite during shearing (Smith et al., 2017). As a consequence, the beam-like calcite fragments will be more likely to rotate so that their c-axes are oriented sub-parallel to σ_1.

4.2. Implications for natural faults

Natural fault gouges and deformation bands are commonly composed of minerals with well-defined cleavage planes (e.g. carbonates, phyllosilicates, amphiboles and feldspars; Faulkner et al., 2011; Demurtas et al., 2016; Smeraglia et al., 2016). Our results suggest that preferential fracturing along cleavage planes can influence fault rock texture, grain size and shape evolution, and microfracture orientations, during faulting and cataclasis in the upper crust (< 2-3 km). This process is likely to be particularly relevant at low strains and in low displacement structures such as deformation bands, where preferential fracturing along cleavage planes could significantly modify pore structure, tortuosity and permeability. For example, Cavailhes and Rotevatn (2018) reported the evolution and deformation mechanisms of deformation bands in tuffaceous volcaniclastic rocks in the Coastal Range of Taiwan. They documented a bimodal grain size distribution during cataclastic flow, with weak volcanic glass composing the fine-grained matrix, and cataclasis of the feldspar, pyroxene and amphibole phenocrysts being mainly controlled by mineralogic cleavage planes. Additionally, our results indicate that low-temperature gouges and cataclasites can develop well-defined CPOs by mechanical grain rotation and fracturing. Further investigation of the role of cleavage and CPO in the mechanical behavior of low-temperature fault zones will provide a more complete understanding of gouge friction evolution in carbonate rocks.

5. Conclusions

Calcite-dolomite gouges deformed experimentally at a range of conditions developed well-defined calcite CPOs during low-temperature cataclasis. The formation of a CPO is interpreted to relate to grain rotation and pervasive fracturing of calcite that occurs preferentially along $\{10\overline{1}4\}$ cleavage planes when the c-axes are oriented sub-parallel to the principal stress. The CPO starts to develop during the earliest stages of shearing when strain and cataclasis are distributed across the full thickness of the gouge layers. Stronger CPOs in calcite are interpreted to reflect a lower fracture energy compared to dolomite. Our results suggest that well-defined CPOs can develop in low-temperature granular fault rocks by mechanical grain rotation and fracturing. Preferential fracturing along cleavage planes can influence the petrophysical and frictional properties of fault rocks during cataclasis in the upper crust.

Acknowledgments

MD, ES and GDT were supported by the European Research Council Consolidator Grant Project No. 614705 NOFEAR. SAFS acknowledges the Marsden Fund Council (project UOO1417) administered by the Royal Society of New Zealand. Leonardo Tauro and Brent Pooley are thanked for assistance during thin section preparation. Marianne Negrini provided assistance with the SEM and EBSD data processing in the Otago Centre for Electron Microscopy, University of Otago. Luiz F.G. Morales and two anonymous reviewers are thanked for providing constructive reviews that helped clarify many aspects of the paper.

References

Abe, S., Mair, K., 2009. Effects of gouge fragment shape on fault friction: New 3D modelling results. Geophys. Res. Lett. 36, 2–5. doi:10.1029/2009GL040684.

Allègre, C.J., Le Mouel, J.L., Provost, A., 1982. Scaling rules in rock fracture and possible implications for earthquake prediction. Nature 297, 47–49. doi:10.1038/297047a0.

Aretusini, S., 2018. Frictional processes of clay-rich gouges at seismic slip rates. PhD Thesis, University of Manchester.

Bachmann, F., Hielscher, R., Schaeben, H., 2010. Texture Analysis with MTEX – Free and Open Source Software Toolbox. Solid State Phenom. 160, 63–68. doi:10.4028/www.scientific.net/SSP.160.63.

Bachmann, F., Hielscher, R., Schaeben, H., 2011. Ultramicroscopy Grain detection from 2d and 3d EBSD data — Specification of the MTEX algorithm. Ultramicroscopy 111, 1720–1733. doi:10.1016/j.ultramic.2011.08.002.

Barrett, S., 2015. Image SXM, http://www.ImageSXM.org.uk.

Bauer, H., Rogowitz, A., Grasemann, B., Decker, K., 2018. Intracrystalline deformation of calcite in the upper brittle crust. Geology 46, 375–378.

Berger, A., Stünitz, H., 1996. Deformation mechanisms and reaction of hornblende: examples from the Bergell tonalite (Central Alps). Tectonophysics 257, 149–174. https://doi.org/10.1016/0040-1951(95)00125-5.

Billi, A., Salvini, F., Storti, F., 2003. The damage zone-fault core transition in carbonate rocks: implications for fault growth, structure and permeability. J. Struct. Geol. 25 (11), 1779-1794.

Billi, A., Storti, F., 2004. Fractal distribution of particle size in carbonate cataclastic rocks from the core of a regional strike-slip fault zone. Tectonophysics 384 (1), 115-128.

Bons, P.D., den Brok, B., 2000. Crystallographic preferred orientation development by dissolution-precipitation creep. J. Struct. Geol. 22, 1713–1722.

Bons, A.-J., Bons, P.D., 2003. The development of oblique preferred orientations in zeolite films and membranes. Microporous Mesoporous Mater. 62, 9–16. doi:10.1016/S1387-1811(03)00384-6.

Bunge, H.J., 1982. Fabric analysis by orientation distribution functions. Tectonophysics, 78, 1.

Burkhard, M., 1993. Calcite twins, their geometry, appearance and significance as stress-strain markers and indicators of tectonic regime: a review. J. Struct. Geol. 15, 351–368.

Cavailhes, T., Rotevatn, A., 2018. Deformation bands in volcaniclastic rocks – Insights from the Shihtiping tuffs, Coastal Range of Taiwan. J. Struct. Geol. 113, 155–175. doi:10.1016/j.jsg.2018.06.004

Chen, X., Madden, A.S., Bickmore, B.R., Reches, Z., 2013. Dynamic weakening by nanoscale smoothing during high-velocity fault slip. Geology 41, 739–742. doi:10.1130/G34169.1

Chen, J., Spiers, C.J., 2016. Rate and state frictional and healing behavior of carbonate fault gouge explained using microphysical model 1–42. doi:10.1002/2016JB013470.

Cladouhos, TT, 1999. Shape preferred orientations of survivor grains in fault gouge. J. Struct. Geol. 21, 419-436.

Crank, J., Nicholson, P., 1947. A practical method for numerical evaluation of solutions of partial differential equations of heat-conduction type. Proceedings of the Cambridge Philosophical Society 43, 50–67.

De Paola, N., Holdsworth, R.E., Viti, C., Collettini, C., Bullock, R., 2015. Can grain size sensitive flow lubricate faults during the initial stages of earthquake propagation? Earth Planet. Sci. Lett. 431, 48–58. doi:10.1016/j.epsl.2015.09.002.

Delle Piane, C., Clennell, M. Ben, Keller, J.V.A., Giwelli, A., Luzin, V., 2017. Carbonate hosted fault rocks: A review of structural and microstructural characteristic with implications for seismicity in the upper crust. J. Struct. Geol. 103, 17–36. doi:10.1016/j.jsg.2017.09.003.

Delle Piane, C., Piazolo, S., Timms, N.E., Luzin, V., Saunders, M., Bourdet, J., Giwelli, A., Clennell, M. Ben, Kong, C., Rickard, W.D.A., Verrall, M., 2018. Generation of amorphous carbon and crystallographic texture during low-temperature subseismic slip in calcite fault gouge.Geology 2–5.

Demurtas, M., Fondriest, M., Balsamo, F., Clemenzi, L., Storti, F., Bistacchi, A., Di Toro, G., 2016. Structure of a normal seismogenic fault zone in carbonates: The Vado di Corno Fault, Campo Imperatore, Central Apennines (Italy). J. Struct. Geol. 90, 185–206. doi:10.1016/j.jsg.2016.08.004.

den Hartog, S.A.M., Spiers, C.J., 2014. A microphysical model for fault gouge friction applied to subduction megathrusts. J. Geophys. Res. Solid Earth 119, 1510–1529. doi:10.1002/2013JB010580.

Di Toro, G., Pennacchioni, G., 2004. Superheated friction-induced melts in zoned pseudotachylytes within the Adamello tonalites (Italian Southern Alps). Journal of Structural Geology 26, 1783-1801.

Di Toro, G., Niemeijer, A., Tripoli, A., Nielsen, S., Di Felice, F., Scarlato, P., Spada, G., Alessandroni, R., Romeo, G., Di Stefano, G., Smith, S., Spagnuolo, E., Mariano, S., 2010. From field geology to earthquake simulation: A new state-of-The-art tool to investigate rock friction during the seismic cycle (SHIVA). Rend. Lincei 21, 95–114. doi:10.1007/s12210-010-0097-x.

Faulkner, D. R., Lewis, A. C., Rutter, E. H., 2003. On the internal structure and mechanics of large strike-slip fault zones: field observations of the Carboneras fault in southeastern Spain. Tectonophysics 367 (3), 235-251. http://dx.doi.org/10.1016/S0040-1951(03)00134-3.

Faulkner, D.R., Mitchell, T.M., Jensen, E., Cembrano, J.M., 2011. Scaling of fault damage zones with displacement and the implications for fault growth processes. J. Geophys. Res. Solid Earth 116, 1–11. doi:10.1029/2010JB007788.

Fourier, J., 1822. Theorie analytique de la chaleur, par M. Fourier. Chez Firmin Didot, père et fils.

Getsinger, A.J., Hirth, G., 2014. Amphibole fabric formation during diffusion creep and the rheology of shear zones. Geology 42, 535–538. https://doi.org/10.1130/G35327.1.

Giuntoli, F., Menegon, L., Warren, C.J., 2018. Replacement reactions and deformation by dissolution and precipitation processes in amphibolites. Journal of Metamorphic Geology 36, 1263–1286. https://doi.org/10.1111/jmg.12445.

Han, R., Shimamoto, T., Hirose, T., Ree, J.-H., Ando, J., 2007. Ultralow Friction of Carbonate Faults Caused by Thermal Decomposition. Science (80-.). 316, 878–881. doi:10.1126/science.1139763.

Hansen, L.N., Zimmerman, M.E., Kohlstedt, D.L., 2011. Grain boundary sliding in San Carlos olivine: Flow law parameters and crystallographic - preferred orientation. J. Geophys. Res. 116. doi:10.1029/2011JB008220.

Hazzard, J.F., Mair, K., 2003. The importance of the third dimension in granular shear. Geophys. Res. Lett. 30, 3–6. doi:10.1029/2003GL017534.

Hielscher, R., Schaeben, H., 2008. A novel pole figure inversion method: specification of the MTEX algorithm. J. Appl. Crystallogr. 41, 1024–1037. doi:10.1107/S0021889808030112.

Jefferies, S.P., Holdsworth, R.E., Shimamoto, T., Takagi, H., Lloyd, G.E., Spiers, C.J., 2006. Origin and mechanical significance of foliated cataclastic rocks in the cores of crustal-scale faults: Examples from the Median Tectonic Line, Japan. J. Geophys. Res. Solid Earth 111, 1–17. doi:10.1029/2005JB004205

Law, R.D., Casey, M., Knipe, R.J., 1986. Kinematic and tectonic significance of microstructures and crystallographic fabrics within quartz mylonites from the Assynt and Eriboll regions of the Moine Thrust Zone, NW Scotland. Trans. R. Soc. Edinburgh Earth Sci. 77, 99–125. doi:10.1017/S0263593300010774.

Mackenzie, J. K., Thomson, M. J., 1957. Some statistics associated with the random disorientation of cubes. Biometrika, 44(1-2), 205-210.

Mair, K., Hazzard, J.F., 2007. Nature of stress accommodation in sheared granular material: Insights from 3D numerical modeling. Earth Planet. Sci. Lett. 259, 469–485. doi:10.1016/j.epsl.2007.05.006.

Muto, J., Nakatani, T., Nishikawa, O., Nagahama, H., 2015. Fractal particle size distribution of pulverized fault rocks as a function of distance from the fault core. Geophys. Res. Lett. 42, 3811–3819. doi:10.1002/2015GL064026.

Niemeijer, A.R., Spiers, C.J., 2007. A microphysical model for strong velocity weakening in phyllosilicate-bearing fault gouges. J. Geophys. Res. Solid Earth 112, 1–12. doi:10.1029/2007JB005008.

Niemeijer, A., G. Di Toro, S. Nielsen, and F. Di Felice, 2011. Frictional melting of gabbro under extreme experimental conditions of normal stress, acceleration, and sliding velocity, J. Geophys. Res., 116, B07404, doi:10.1029/2010JB008181.

Okamoto, A., Sekine, K., 2011. Textures of syntaxial quartz veins synthesized by hydrothermal experiments. J. Struct. Geol. 33, 1764–1775. doi:10.1016/j.jsg.2011.10.004.

Passchier, C., Trouw, R., 2005. Microtectonics. Springer-Verlag, Berlin Heidelberg 366 pp.

Pearce, M.A., Timms, N.E., Hough, R.M., Cleverley, J.S., 2013. Reaction mechanism for the replacement of calcite by dolomite and siderite: Implications for geochemistry, microstructure and porosity evolution during hydrothermal mineralisation. Contrib. to Mineral. Petrol. 166, 995–1009. doi:10.1007/s00410-013-0905-2.

Philpotts, A.R., 1990. Principles of Igneous and Metamorphic Petrology, Prentice Hall, Englewood Cliffs.

Pozzi, G., De Paola, N., Holdsworth, R. E., Bowen, L., Nielsen, S. B., & Dempsey, E. D., 2019. Coseismic ultramylonites: An investigation of nanoscale viscous flow and fault weakening during seismic slip. Earth and Planetary Science Letters, 516, 164-175.

Power, W.L., Tullis, T.E., 1989. The relationship between slickenside surfaces in fine-grained quartz and the seismic cycle. J. Struct. Geol. 11, 879–893. doi:10.1016/0191-8141(89)90105-3.

Prior, D.J., Boyle, A.P., Brenker, F., Cheadle, M.C., Day, A., Lopez, G., Peruzzo, L., Potts, G.J., Reddy, S., Spiess, R., Timms, N.E., Trimby, P.W., Wheeler, J., Zetterström, L., 1999. The application of electron backscatter diffraction and orientation constrast imaging in th SEM to textural problems in rocks. Am. Mineral. 84, 1741–1759. doi:10.2138/am-1999-11-1204.

Ree, J.H., Ando, J., Han, R., Shimamoto, T., 2014. Coseismic microstructures of experimental fault zones in Carrara marble. J. Struct. Geol. 66, 75–83. doi:10.1016/j.jsg.2014.05.012.

Rempe, M., Smith, S., Mitchell, T., Hirose, T., Di Toro, G., 2017. The effect of water on strain localization in calcite fault gouge sheared at seismic slip rates. J. Struct. Geol. 97, 104–117. doi:10.1016/j.jsg.2017.02.007.

Rowe, K.J., Rutter, E.H., 1990. Palaeostress estimation using calcite twinning. Experimental calibration and application to nature. J. Struct. Geol. 12, 1–17. doi:10.1016/0191-8141(90)90044-Y.

Røyne, A., Bisschop, J., and Dysthe, D. K., 2011. Experimental investigation of surface energy and subcritical crack growth in calcite. Journal of Geophysical Research: Solid Earth (1978 – 2012), 116(B4).

Rutter, E.H., Faulkner, D.R., Brodie, K.H., Phillips, R.J., Searle, M.P., 2007. Rock deformation processes in the Karakoram fault zone, Eastern Karakoram, Ladakh, NW India. J. Struct. Geol. 29, 1315–1326. doi:10.1016/j.jsg.2007.05.001.

Sammis, C., King, G., Biegel, R., 1987. The kinematics of gouge deformation. Pure Appl. Geophys. 125, 777–812. doi:10.1007/BF00878033.

Sammis, C.G., King, G.C.P., 2007. Mechanical origin of power law scaling in fault zone rock. Geophys. Res. Lett. 34, 2–5. doi:10.1029/2006GL028548.

Samtani, M., Dollimore, D., Alexander, K.S., 2002. Comparison of dolomite decomposition kinetics with related carbonates and the effect of procedural variables on its kinetic parameters. Thermochim. Acta 393, 135–145.

Schröckenfuchs, T., Bauer, H., Grasemann, B., Decker, K., 2015. Rock pulverization and localization of a strike-slip fault zone in dolomite rocks (Salzach–Ennstal–Mariazell–Puchberg fault, Austria). J. Struct. Geol. 78, 67-85.

Smeraglia, L., Aldega, L., Billi, A., Carminati, E., Doglioni, C., 2016. Phyllosilicate injection along extensional carbonate-hosted faults and implications for co-seismic slip propagation: Case studies from the central Apennines, Italy. J. Struct. Geol. 93, 29–50. doi:10.1016/j.jsg.2016.10.003.

Smith, S.A.F., Billi, A., di Toro, G., Spiess, R., 2011. Principal Slip Zones in Limestone: Microstructural Characterization and Implications for the Seismic Cycle (Tre Monti Fault, Central Apennines, Italy). Pure Appl. Geophys. 168, 2365–2393. doi:10.1007/s00024-011-0267-5.

Smith, S.A.F., Di Toro, G., Kim, S., Ree, J.H., Nielsen, S., Billi, A., Spiess, R., 2013. Coseismic recrystallization during shallow earthquake slip. Geology 41, 63–66. doi:10.1130/G33588.1.

Smith, S.A.F., Nielsen, S., Di Toro, G., 2015. Strain localization and the onset of dynamic weakening in calcite fault gouge. Earth Planet. Sci. Lett. 413, 25–36. doi:10.1016/j.epsl.2014.12.043.

Smith, S.A.F., Griffiths, J.R., Fondriest, M., Di Toro, G., 2017. "Coseismic Foliations" in Gouge and Cataclasite: Experimental Observations and Consequences for Interpreting the Fault Rock Record. In: Fault Zone Dynamic Processes: Evolution of Fault Properties During Seismic Rupture. Thomas, M.Y., Mitchell, T.M. & Bhat, H.S. (eds). Monograph of the American Geophysical Union, Number 227, pp 81–102.

Snoke, A.W., Tullis, J., Todd, V.R., 1998. Fault-Related Rocks: a Photographic Atlas. Princeton Univ. Press, Princeton, N.J.

Spiess, R., Peruzzo, L., Prior, D.J., Wheeler, J., 2001. Development of garnet porphyroblasts by multiple nucleation , coalescence and boundary misorientation-driven rotations. J. Metamorph. Geol. 19, 269–290.

Toy, V.G., Mitchell, T.M., Druiventak, A., Wirth, R., 2015. Crystallographic preferred orientations may develop in nanocrystalline materials on fault planes due to surface energy interactions. Geochemistry, Geophys. Geosystems 16, 2549–2563. doi:10.1002/2015GC005857.

Turcotte, D.L., 1986. Fractals and Fragmentation. J. Geophys. Res. 91, 1921–1926.

Verberne, B.A., de Bresser, J.H.P., Niemeijer, A.R., Spiers, C.J., de Winter, D.A.M., Plümper, O., 2013. Nanocrystalline slip zones in calcite fault gouge show intense crystallographic preferred orientation: Crystal plasticity at subseismic slip rates at 18-150 °C. Geology 41, 863–866. doi:10.1130/G34279.1.

Violay, M., Nielsen, S., Gibert, B., Spagnuolo, E., Cavallo, A., Azais, P., Vinciguerra, S., Di Toro, G., 2014. Effect of water on the frictional behavior of cohesive rocks during earthquakes. Geology 42, 27–30. doi:10.1130/G34916.1.

Wenk, H.-R., Christie, J.M., 1991. Comments on the interpretation of deformation textures in rocks. J. Struct. Geol. 13, 1091–1110.

Wheeler, J., Prior, D.J., Jiang, Z., Spiess, R., Trimby, P.W., 2001. The petrological significance of misorientations between grains. Contrib. to Mineral. Petrol. 141, 109–124. doi:10.1007/s004100000225.

Zhang, S., Karato, S., 1995. Lattice preferred orientation of olivine aggregates deformed in simple shear. Nature 375, 774–777.

Figure captions

Figure 1. Experimental setup and starting materials. a) Backscattered scanning electron microscope image of the starting materials composed of 50 wt.% calcite and 50 wt.% dolomite. b) Scale diagram of gouge holder with main parts labelled (modified after Smith et al., 2017). c) Montage of the recovered sample from experiment *s1218* (Table 1). EBSD analysis in each sample was focused on the bulk gouge (dashed orange rectangle) at distances > 400-500 µm from the principal slip zone. The sinusoids adjacent to the sample montage represent the grooves in the sample holder. Inset shows the geometry of the annular gouge layer. Thin sections were cut tangential to the slip vector, d) Schematic diagram of the shear strain distribution in the gouge layer during rotary-shear experiments, as described in Rempe et al. (2017) and Smith et al. (2017). The analyzed areas are characterized by relatively low finite shear strains, usually < 2-2.5.

Figure 2. Summary of mechanical data from calcite-dolomite mixtures. The apparent friction coefficient (μ) exhibited slip-strengthening for slip rates ≤ 0.01 ms^{-1}. At 1 ms^{-1} the gouges showed dynamic weakening with steady state friction coefficient of μ = 0.28 in both room-humidity and water-dampened conditions.

Figure 3. Microstructural analysis and measurements of fracture and twin orientations in calcite after a) application of uniaxial stress and b)-e) shearing. Traces of fractures and twins were identified from the band contrast maps. f) SEM-BSE image showing fractures (red lines) that formed during uniaxial stress under water-dampened conditions. g) Pervasive fracturing (red lines) in calcite grains after shearing. Fractures often exploit $\{10\overline{1}4\}$ cleavage *r*-rhomb planes. h) Development of a foliation in the bulk gouge consisting of compositional banding was observed after high-velocity slip (1 ms^{-1}) under room-humidity conditions. In f)-g) and h) calcite is white and dolomite is grey. i) Band

contrast image of calcite grains that exhibit one twin set, which is typically orientated synthetic to the shear sense.

Figure 4. Calcite grain shape analysis for grains with aspect ratio ≥ 1.5 after a) application of uniaxial stress (experiment *slw*, grains = 1343) and b) shearing (experiment *s1217*, grains = 1327). Orientations of grain long axes are given as counterclockwise (CCW) from the gouge layer boundaries. Arrows on SEM images highlight the main fracture sets. In the case of the sheared gouges, the fractures are strongly aligned. On the histogram, the orientation of the mode of the calcite c-axis CPO (from Figure 6a) is also shown.

Figure 5. Cleavage-controlled fracturing in calcite grains. a) Detail of a calcite grain that fractured during shearing (experiment *s1217*). In the SEM-BSE image calcite is white and dolomite is grey. b) IPFz coloring of the analyzed calcite grain (z corresponds to the direction orthogonal to the thin section plane). The colored calcite crystals show the orientation in space of the $\{10\bar{1}4\}$ cleavage planes and the $\{10\bar{1}0\}$ prisms in the four orientation domains labelled on the EBSD map. c) Stereonets of the analyzed calcite grain (one point per pixel) for a series of crystallographic planes and directions. The rose diagram inside the pole figures corresponds to the orientation of the fracture traces. For the $\{10\bar{1}4\}$ cleavage plane, the colored lines outside the pole figure represent the strike of the cleavage planes determined from the poles.

Figure 6. CPO data for calcite and dolomite grains from mixed calcite-dolomite experiments over a wide range of experimental conditions, as well as pure calcite and dolomite gouges. Values are scaled to the highest multiple of a uniform distribution (m.u.d.) value observed in the experiment at 1 ms^{-1} in room-humidity conditions (i.e., m.u.d. = 2.8). Maximum m.u.d. values are annotated

next to each pole figure. a) All CPO data were collected from experiments in which the gouge was deformed for 0.4 m, with the exception of experiments performed under room-humidity conditions at 30 μms^{-1} (*s1322*) and 0.001 ms^{-1} (*s1323*) that were sheared for 0.1 m (see asterisks next to pole figures). b-d) Misorientation angle distribution analysis for calcite in the b) uniaxial stress experiment, c) experiment *s1214* deformed at 30 μms^{-1} and d) experiment *s1221* deformed at 1 ms^{-1}. For neighbor- and random-pair grains, histogram bins are 5 degrees.

Figure 7. Evolution of calcite CPO with increasing displacement. Pole figures show contours for the calcite (0001) plane. Data curves show the friction coefficient for the four experiments performed under identical deformation conditions and increasing displacements. Maximum m.u.d. values are annotated next to each pole figure.

Figure 8. Crystallographic preferred orientation for near-equant calcite grains in experiment *s1217*. a) Map highlighting the distribution in the bulk gouge of calcite grains with an aspect ratio < 1.5. b) Calcite orientation data for grains shown in (a). Maximum m.u.d. values are annotated next to each pole figure.

Figure 9. Thermocouple measurements of temperature evolution with time or slip. The plots show temperature data from the thermocouple located nearest to the gouge layer (see location in Figure 1b). In parts a) and b) temperatures are shown against time due to the slow duration of the experiments and the low data acquisition rate of the thermocouples (i.e., 2.5 Hz).

Figure 10. Thermal modelling of heat diffusion in the bulk gouge. a) Temperature evolution with time at different locations in the gouge layer for experiment *s1221* according to the Crank and

Nicholson finite difference method (1947). At the end of slip, at t = 0 s, the principal slip zone (PSZ) is assumed to be c. 160 µm thick with an initial T of 620 °C. The bulk gouge (2.5 mm thick) and the gouge holder have an ambient temperature of 20 °C (room temperature). Temperature evolution is modeled at four different time intervals of 0.01, 0.1, 0.5 and 1 s. The box to the right highlights the gouge domain where the CPO of the calcite grains was measured. b) Results of the thermal model for temperature increase in the gouge layer from slip initiation (t = 0 s) to 0.6 s after the end of slip (t = 1 s). The principal slip zone (160 µm thick) is heated at 620 °C for 0.05 s (corresponding to c. 4-5 cm of slip at a slip rate of 1 ms^{-1}) from the onset of slip. The box to the right highlights the gouge domain where the CPO of the calcite grains was measured.

Figure 11. Brittle deformation in the gouge at different displacements (*d*), slip rates (*V*) and deformation conditions (room-humidity, *RH*, vs. water-dampened, *WD*) at constant normal load of 17.5 MPa. a) Experiment *s1212*: *V* = 0.001 ms^{-1}, *d* = 0.4 m, *RH*. b) Experiment *s1213*: *V* = 0.001 ms^{-1}, *d* = 0.4 m, *WD*. c) Experiment *s1217*: *V* = 0.01 ms^{-1}, *d* = 0.4 m, *RH*. d) Experiment *s1220*: *V* = 0.1 ms^{-1}, *d* = 0.4 m, *WD*. e) Experiment *s1222*: *V* = 1 ms^{-1}, *d* = 0.4 m, *WD*. f) Experiment *s1322*: *V* = 30 μms^{-1}, *d* = 0.1 m, *RH*.

Figure 12. Conceptual model for the development of a CPO in sheared granular calcite. The model summarizes the main results from EBSD analysis of calcite CPOs (stereoplots) and image analysis of calcite twin and fracture orientations (rose diagrams) for a) uniaxial loading and b) shearing at a wide range of slip rates and displacements. The middle boxes show schematic illustrations of calcite grains microstructure in the gouge, illustrating the orientation of twins and fractures and, after shear, the preservation of calcite c-axes in an orientation subparallel to the predicted σ_1 orientation.

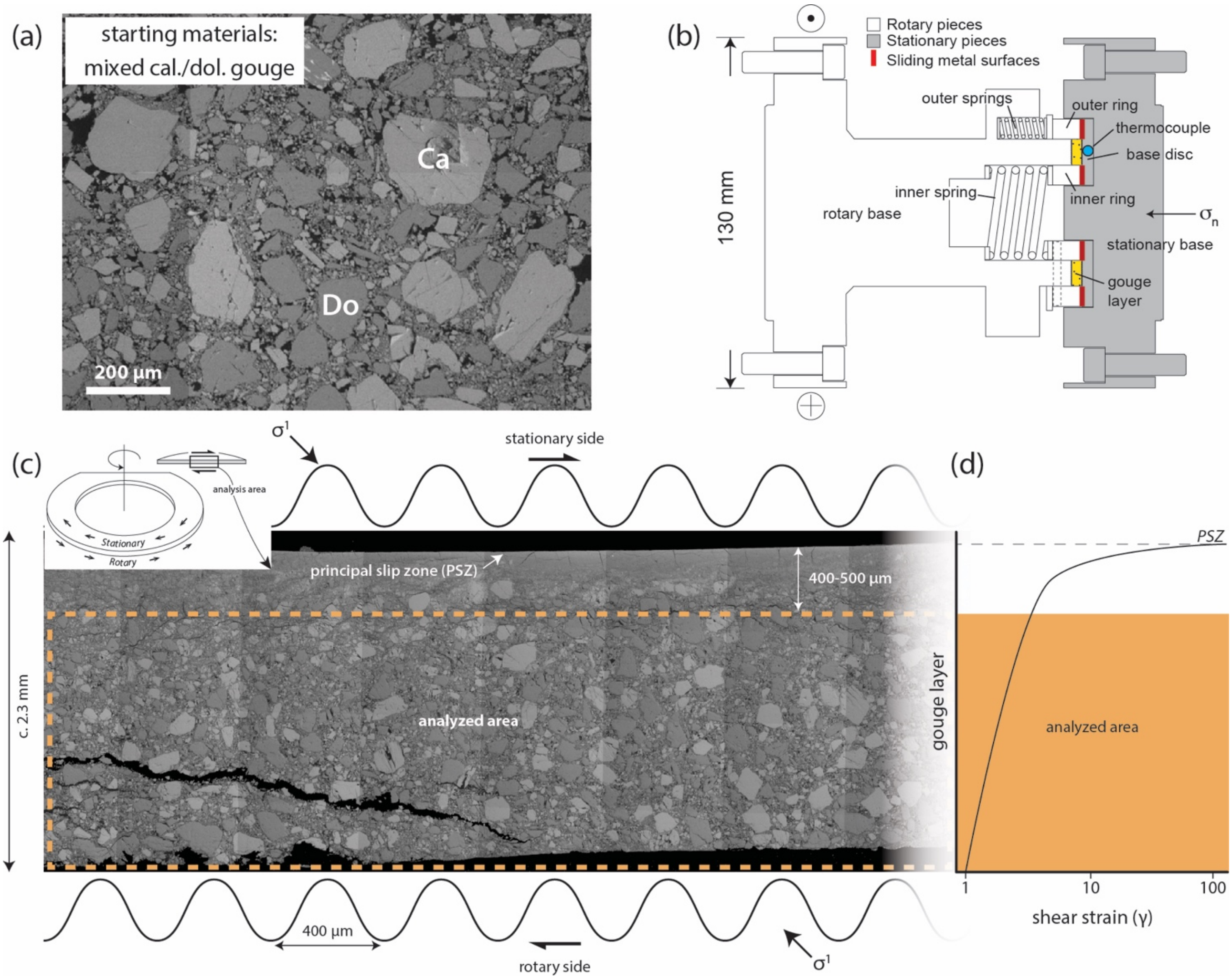

Figure 1. Experimental setup and starting materials. a) Backscattered scanning electron microscope image of the starting materials composed of 50 wt.% calcite and 50 wt.% dolomite. b) Scale diagram of gouge holder with main parts labelled (modified after Smith et al., 2017). c) Montage of the recovered sample from experiment *s1218* (Table 1). EBSD analysis in each sample was focused on the bulk gouge (dashed orange rectangle) at distances > 400-500 µm from the principal slip zone. The sinusoids adjacent to the sample montage represent the grooves in the sample holder. Inset shows the geometry of the annular gouge layer. Thin sections were cut tangential to the slip vector, d) Schematic diagram of the shear strain distribution in the gouge layer during rotary-shear experiments, as described in Rempe et al. (2017) and Smith et al. (2017). The analyzed areas are characterized by relatively low finite shear strains, usually < 2-2.5.

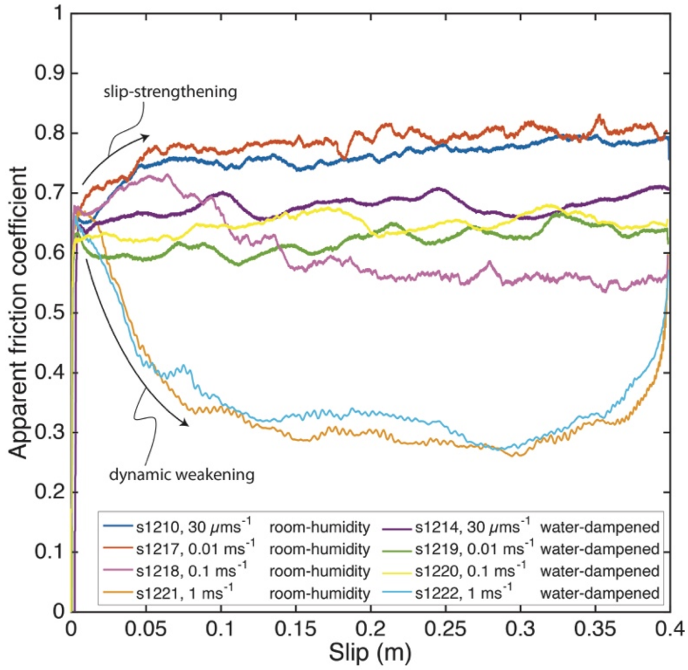

Figure 2. Summary of mechanical data from calcite-dolomite mixtures. The apparent friction coefficient (μ) exhibited slip-strengthening for slip rates ≤ 0.01 ms^{-1}. At 1 ms^{-1} the gouges showed dynamic weakening with steady state friction coefficient of μ = 0.28 in both room-humidity and water-dampened conditions.

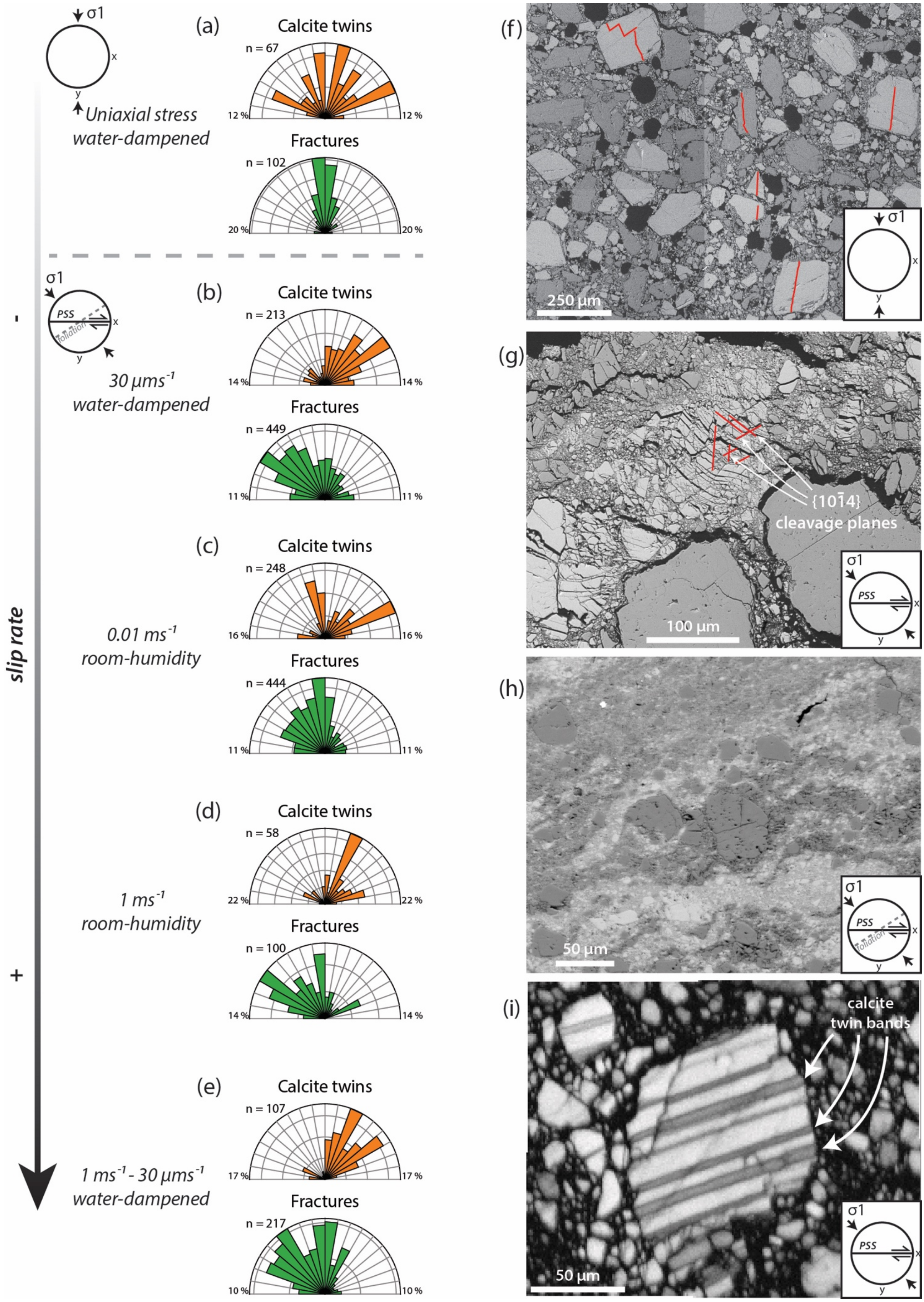

Figure 3. Microstructural analysis and measurements of fracture and twin orientations in calcite after a) application of uniaxial stress and b)-e) shearing. Traces of fractures and twins were identified

from the band contrast maps. f) SEM-BSE image showing fractures (red lines) that formed during uniaxial stress under water-dampened conditions. g) Pervasive fracturing (red lines) in calcite grains after shearing. Fractures often exploit $\{10\bar{1}4\}$ cleavage *r*-rhomb planes. h) Development of a foliation in the bulk gouge consisting of compositional banding was observed after high-velocity slip (1 ms^{-1}) under room-humidity conditions. In f)-g) and h) calcite is white and dolomite is grey. i) Band contrast image of calcite grains that exhibit one twin set, which is typically orientated synthetic to the shear sense.

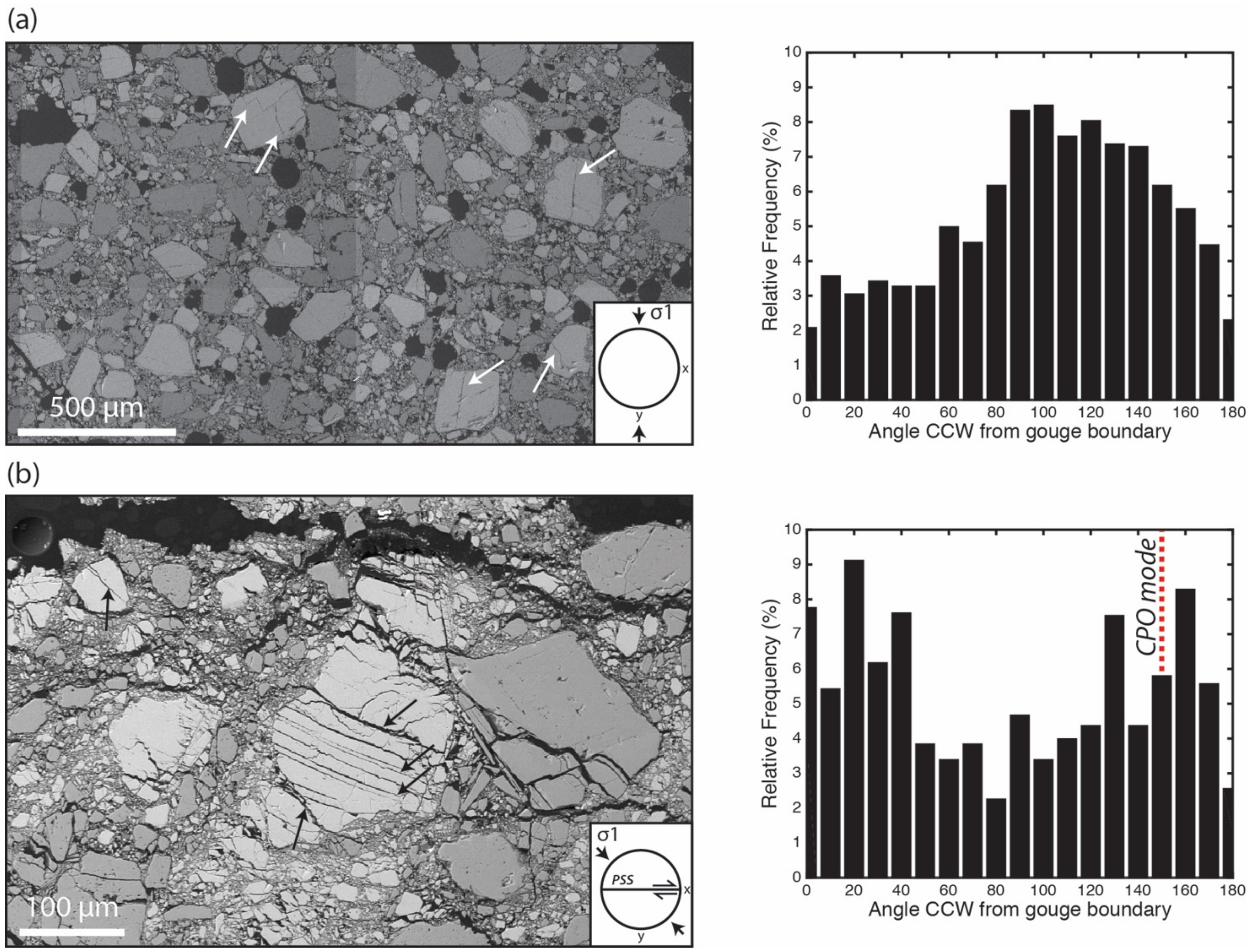

Figure 4. Calcite grain shape analysis for grains with aspect ratio ≥ 1.5 after a) application of uniaxial stress (experiment *slw*, grains = 1343) and b) shearing (experiment *s1217*, grains = 1327). Orientations of grain long axes are given as counterclockwise (CCW) from the gouge layer boundaries. Arrows on SEM images highlight the main fracture sets. In the case of the sheared gouges, the fractures are strongly aligned. On the histogram, the orientation of the mode of the calcite c-axis CPO (from Figure 6a) is also shown.

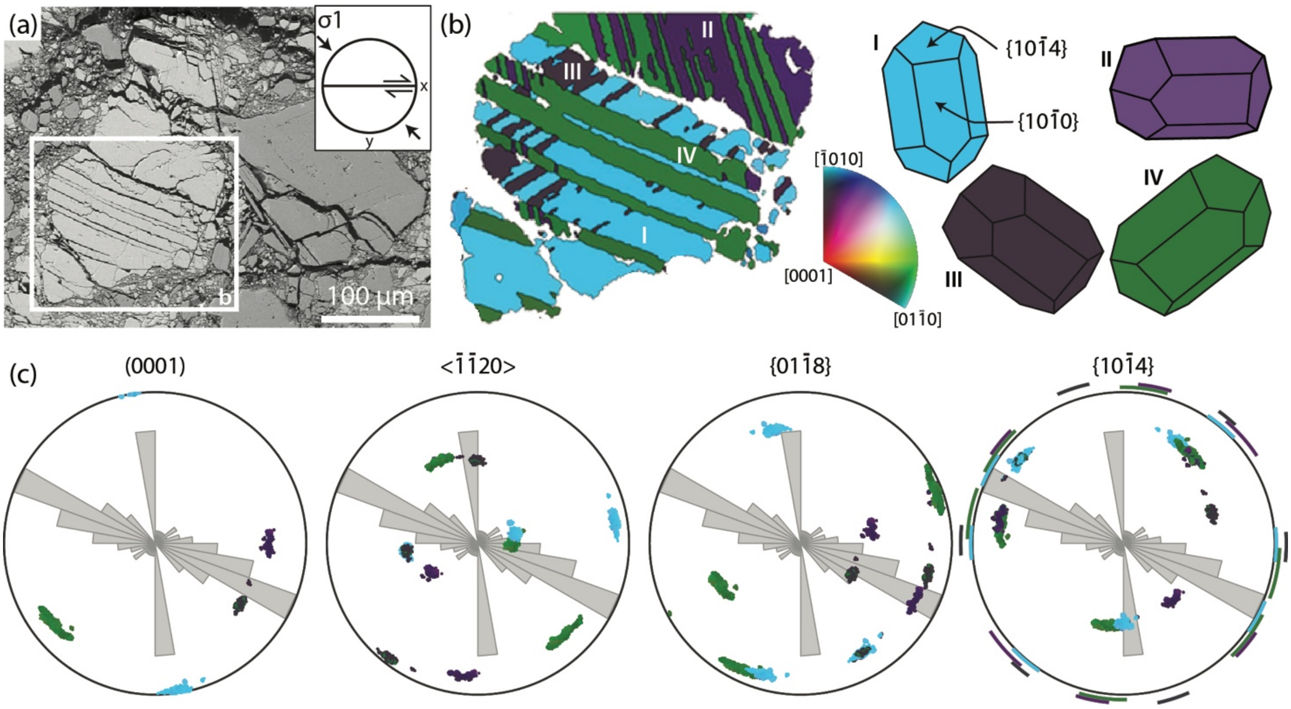

Figure 5. Cleavage-controlled fracturing in calcite grains. a) Detail of a calcite grain that fractured during shearing (experiment *s1217*). In the SEM-BSE image calcite is white and dolomite is grey. b) IPFz coloring of the analyzed calcite grain (z corresponds to the direction orthogonal to the thin section plane). The colored calcite crystals show the orientation in space of the $\{10\overline{1}4\}$ cleavage planes and the $\{10\overline{1}0\}$ prisms in the four orientation domains labelled on the EBSD map. c) Stereonets of the analyzed calcite grain (one point per pixel) for a series of crystallographic planes and directions. The rose diagram inside the pole figures corresponds to the orientation of the fracture traces. For the $\{10\overline{1}4\}$ cleavage plane, the colored lines outside the pole figure represent the strike of the cleavage planes determined from the poles.

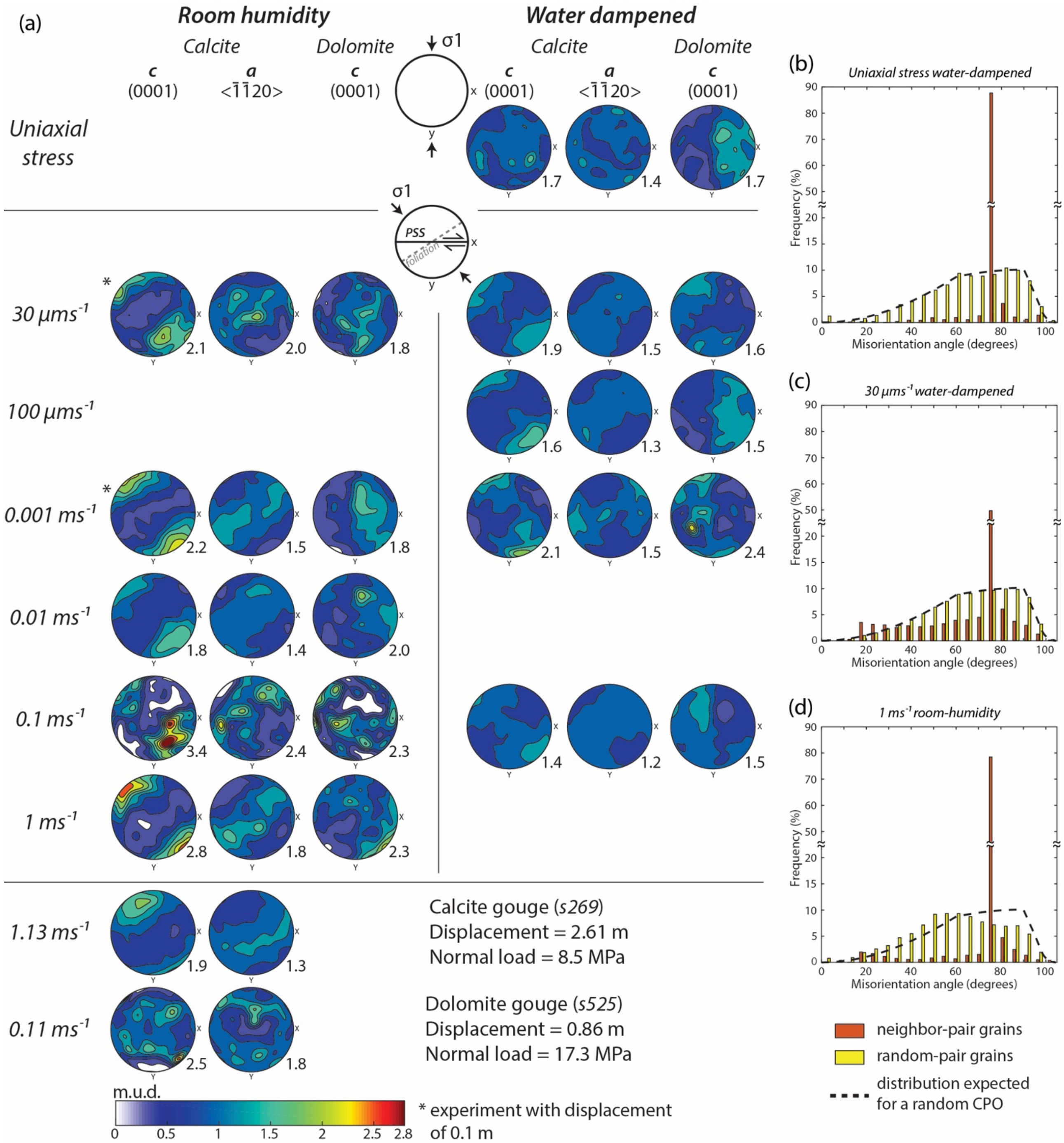

Figure 6. CPO data for calcite and dolomite grains from mixed calcite-dolomite experiments over a wide range of experimental conditions, as well as pure calcite and dolomite gouges. Values are scaled to the highest multiple of a uniform distribution (m.u.d.) value observed in the experiment at 1 ms^{-1} in room-humidity conditions (i.e., m.u.d. = 2.8). Maximum m.u.d. values are annotated next to each pole figure. a) All CPO data were collected from experiments in which the gouge was deformed for 0.4 m, with the exception of experiments performed under room-humidity conditions at 30 μms^{-1} (*s1322*) and 0.001 ms^{-1} (*s1323*) that were sheared for 0.1 m (see asterisks next to pole figures). b-d) Misorientation angle distribution analysis for calcite in the b) uniaxial stress experiment, c) experiment *s1214* deformed at 30 μms^{-1} and d) experiment *s1221* deformed at 1 ms^{-1}. For neighbor- and random-pair grains, histogram bins are 5 degrees.

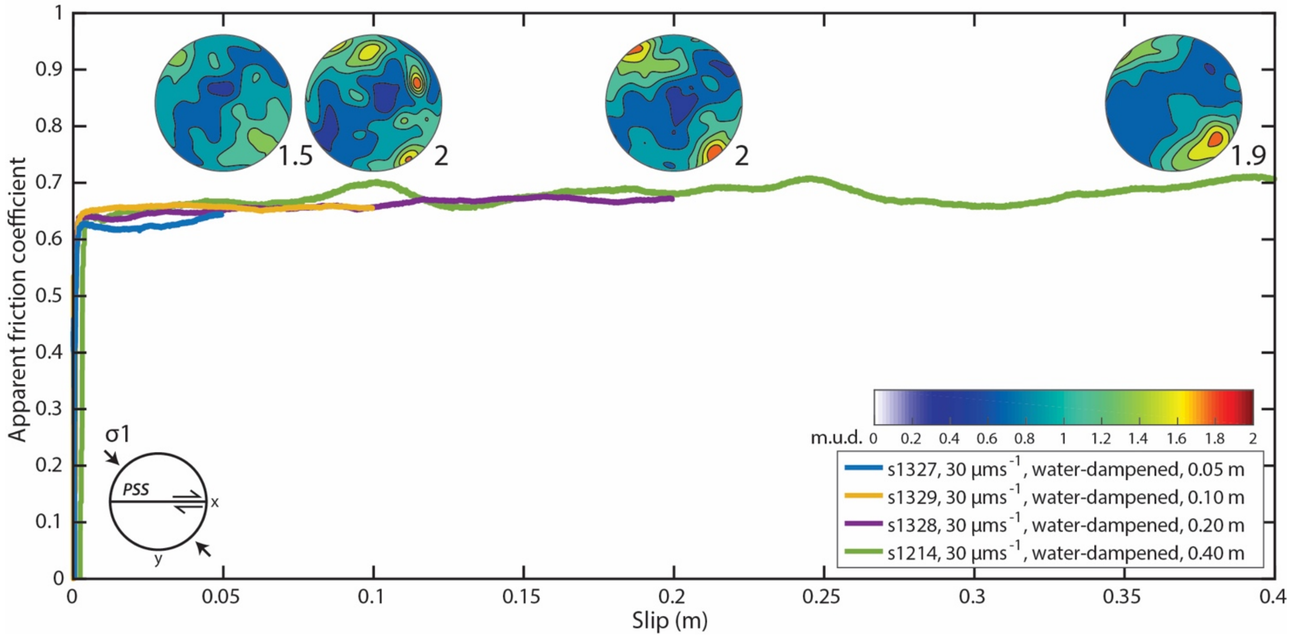

Figure 7. Evolution of calcite CPO with increasing displacement. Pole figures show contours for the calcite (0001) plane. Data curves show the friction coefficient for the four experiments performed under identical deformation conditions and increasing displacements. Maximum m.u.d. values are annotated next to each pole figure.

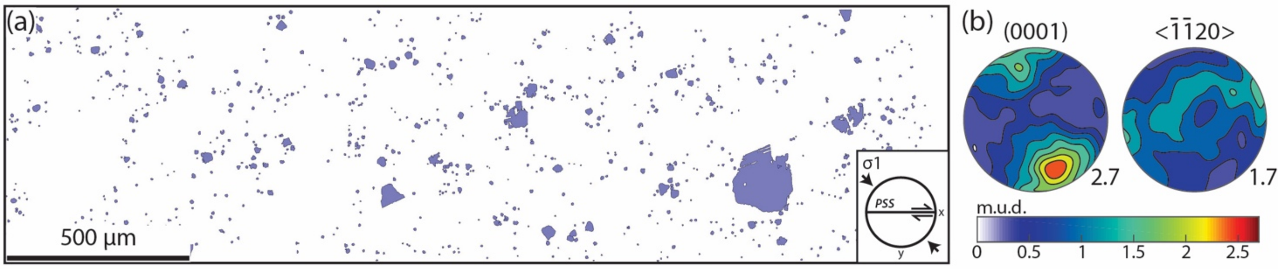

Figure 8. Crystallographic preferred orientation for near-equant calcite grains in experiment *s1217*. a) Map highlighting the distribution in the bulk gouge of calcite grains with an aspect ratio < 1.5. b) Calcite orientation data for grains shown in (a). Maximum m.u.d. values are annotated next to each pole figure.

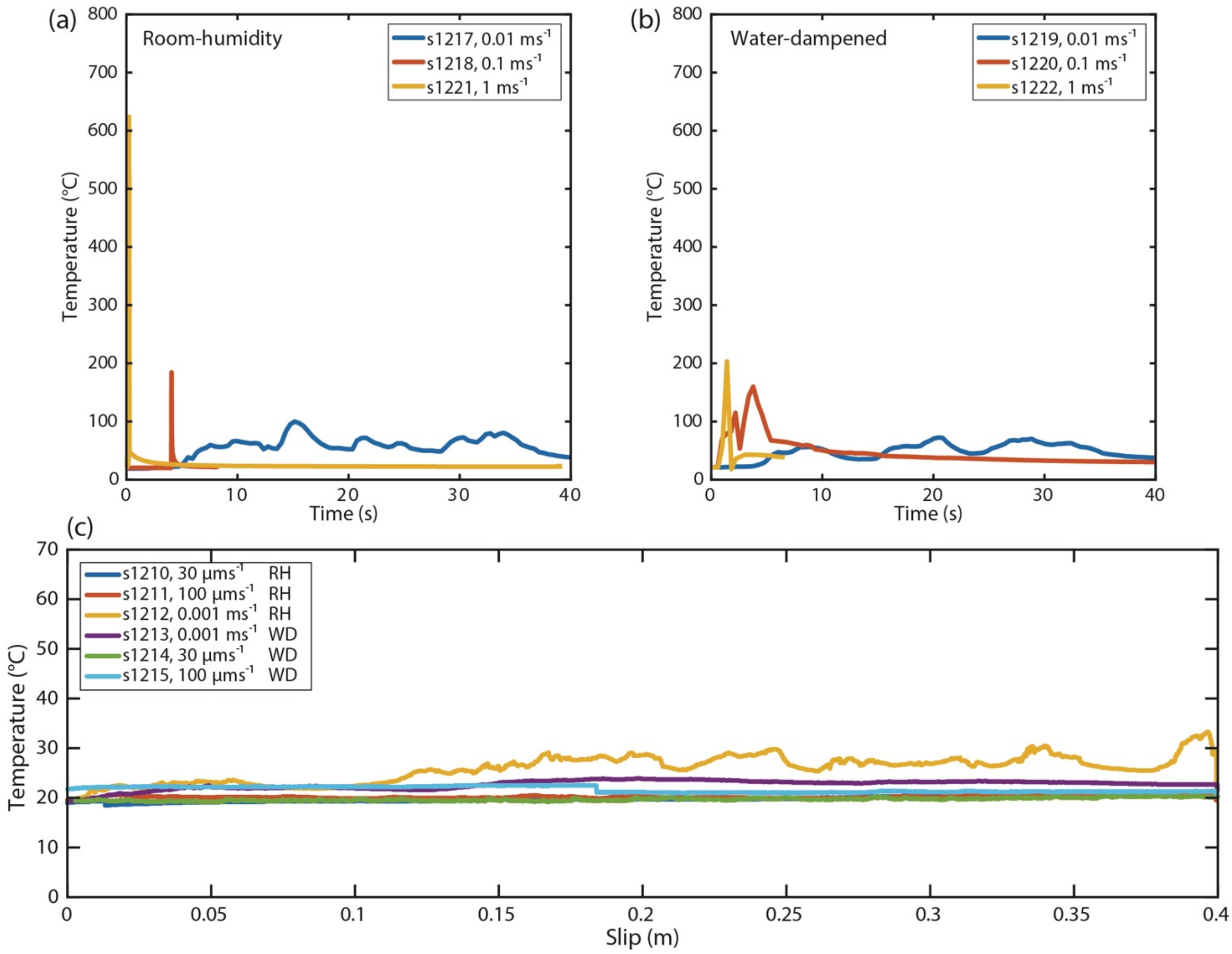

Figure 9. Thermocouple measurements of temperature evolution with time or slip. The plots show temperature data from the thermocouple located nearest to the gouge layer (see location in Figure 1b). In parts a) and b) temperatures are shown against time due to the slow duration of the experiments and the low data acquisition rate of the thermocouples (i.e., 2.5 Hz).

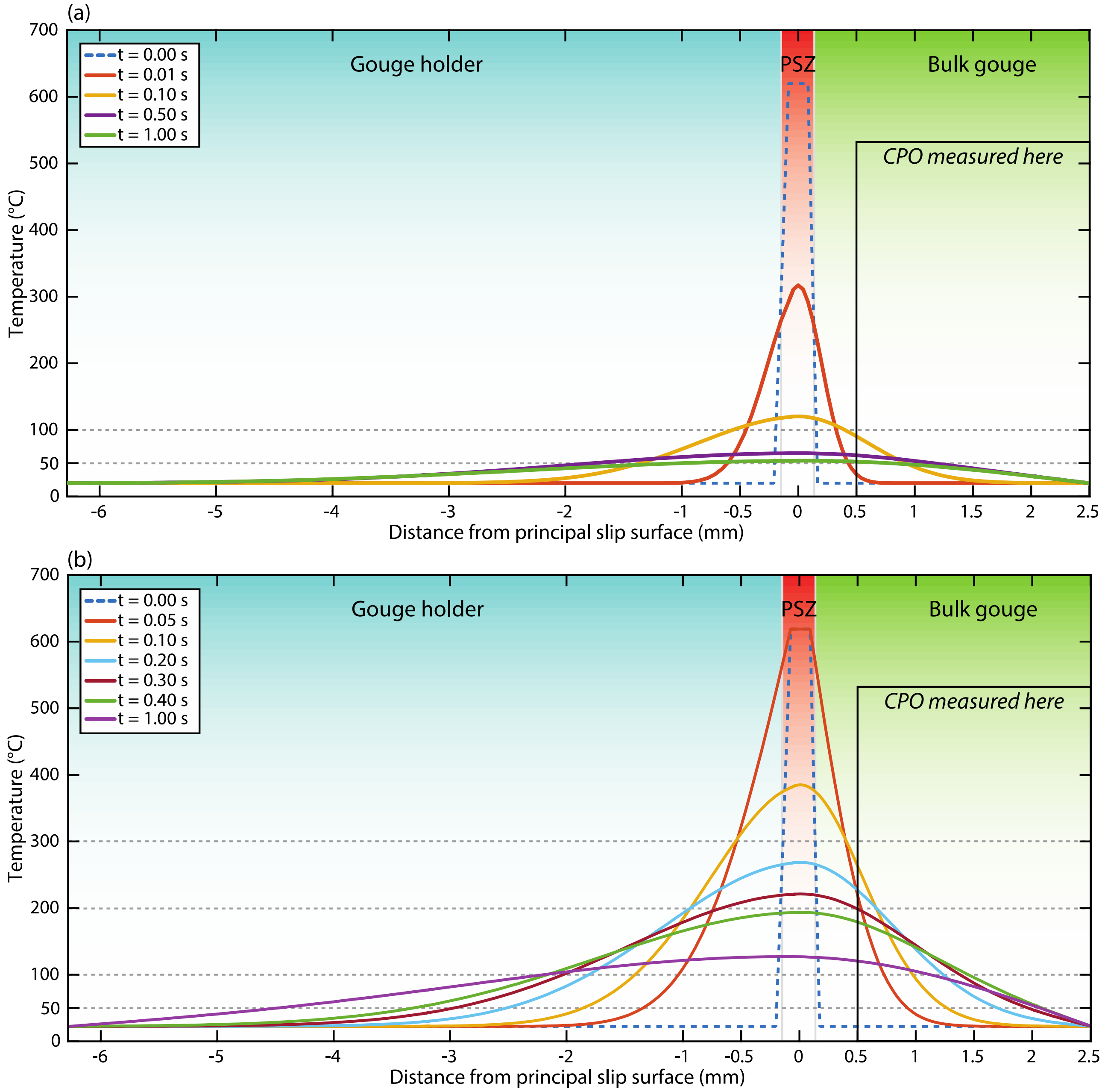

Figure 10. Thermal modelling of heat diffusion in the bulk gouge. a) Temperature evolution with time at different locations in the gouge layer for experiment *s1221* according to the Crank and Nicholson finite difference method (1947). At the end of slip, at t = 0 s, the principal slip zone (PSZ) is assumed to be c. 160 µm thick with an initial T of 620 °C. The bulk gouge (2.5 mm thick) and the gouge holder have an ambient temperature of 20 °C (room temperature). Temperature evolution is modeled at four different time intervals of 0.01, 0.1, 0.5 and 1 s. The box to the right highlights the gouge domain where the CPO of the calcite grains was measured. b) Results of the thermal model for temperature increase in the gouge layer from slip initiation (t = 0 s) to 0.6 s after the end of slip (t = 1 s). The principal slip zone (160 µm thick) is heated at 620 °C for 0.05 s (corresponding to c. 4-5 cm of slip at a slip rate of 1 ms^{-1}) from the onset of slip. The box to the right highlights the gouge domain where the CPO of the calcite grains was measured.

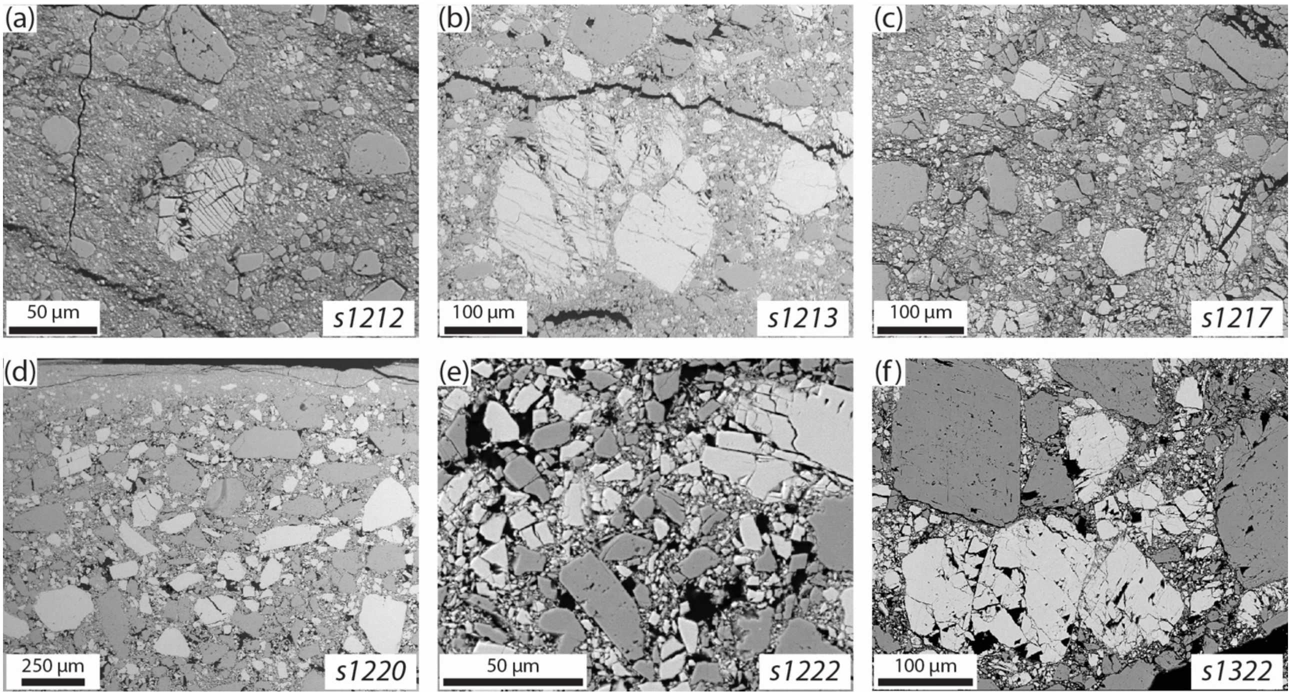

Figure 11. Brittle deformation in the gouge at different displacements (*d*), slip rates (*V*) and deformation conditions (room-humidity, *RH*, vs. water-dampened, *WD*) at constant normal load of 17.5 MPa. a) Experiment *s1212*: V = 0.001 ms^{-1}, d = 0.4 m, *RH*. b) Experiment *s1213*: V = 0.001 ms^{-1}, d = 0.4 m, *WD*. c) Experiment *s1217*: V = 0.01 ms^{-1}, d = 0.4 m, *RH*. d) Experiment *s1220*: V = 0.1 ms^{-1}, d = 0.4 m, *WD*. e) Experiment *s1222*: V = 1 ms^{-1}, d = 0.4 m, *WD*. f) Experiment *s1322*: V = 30 μms^{-1}, d = 0.1 m, *RH*.

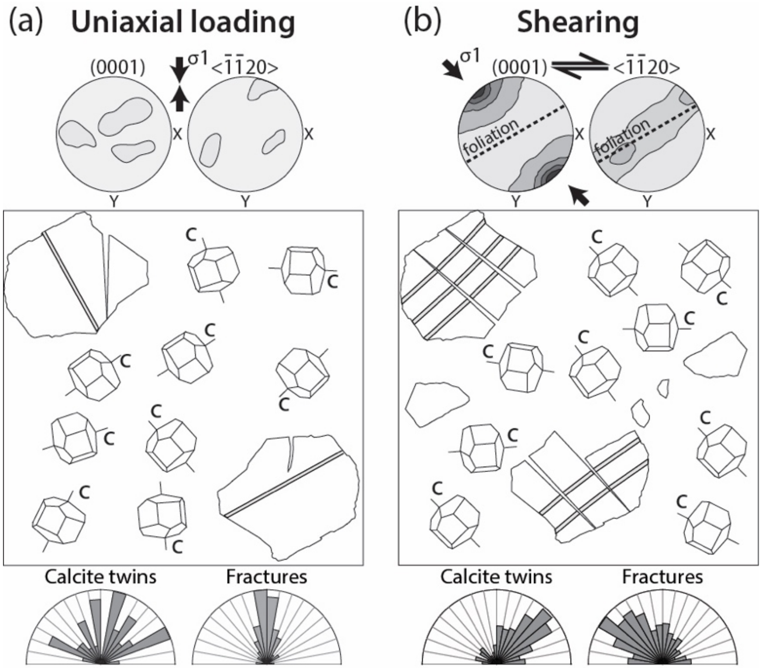

Figure 12. Conceptual model for the development of a CPO in sheared granular calcite. The model summarizes the main results from EBSD analysis of calcite CPOs (stereoplots) and image analysis of calcite twin and fracture orientations (rose diagrams) for a) uniaxial loading and b) shearing at a wide range of slip rates and displacements. The middle boxes show schematic illustrations of calcite grains microstructure in the gouge, illustrating the orientation of twins and fractures and, after shear, the preservation of calcite c-axes in an orientation subparallel to the predicted σ_1 orientation.

	Experiment	*Target slip rate* *m s^{-1}*	*Displacement* *m*	*Normal stress* *MPa*
Room-humidity				
	s1322	0.00003	0.1	17.5
	s1211*	0.0001	0.4	17.5
	s1323	0.001	0.1	17.5
	s1212*	0.001	0.4	17.5
	s1217	0.01	0.4	17.5
	s1218	0.1	0.4	17.5
	s1221	1	0.4	17.5
Water-dampened				
	s1327	0.00003	0.05	17.5
	s1329	0.00003	0.1	17.5
	s1328	0.00003	0.2	17.5
	s1214	0.00003	0.4	17.5
	s1215	0.0001	0.4	17.5
	s1213	0.001	0.4	17.5
	s1219*	0.01	0.4	17.5
	s1220	0.1	0.4	17.5
	s1222*	1	0.4	17.5
Uniaxial compression water-dampened	slw			17.5
Calcite Room-humidity	s269	1.13	2.61	*8.5*
Dolomite Room-humidity	s525	0.11	0.86	17.3

Table 1. Summary of experiments analyzed in this study. *EBSD analysis not performed.

Supplementary material

“Development of crystallographic preferred orientation during cataclasis in low-temperature carbonate fault gouge”

Matteo Demurtas *, Steven A. F. Smith, David J. Prior, Elena Spagnuolo, Giulio Di Toro

* Corresponding author: Matteo Demurtas (matteo.demurtas@geo.uio.no)

1. EBSD data cleaning and processing in MTEX

Given the difficulty of the analyzed material (i.e., fine-grained porous fault gouge) and the systematic misindexing that occurs between calcite and dolomite, the standard data cleaning and processing routine with CHANNEL5 software (from HKL Technology, Oxford Instruments) did not yield accurate crystallographic orientation data. Therefore, data cleaning and processing was carried out with MTEX (Bachmann et al., 2010).

For our analysis, a new workflow was created to deal with the systematic calcite/dolomite misindexing in the raw EBSD data by using EDS maps (Fig. S1). Since in our case the EDS analysis does not yield quantitative element analysis, the elemental maps did not allow us to recognize the mineral phase by their absolute elemental values. Therefore, the reassignment of the correct phase to the misindexed pixel was done by setting a threshold for each phase on a Mg/Ca map, with peak intensity ratios of Mg/Ca ≥ 0.2 for dolomite and Mg/Ca ≤ 0.15 for calcite (note: ratios used here were not stoichiometric; Fig. S1d-f). During this step, non-indexed pixels remained unchanged. For each indexed pixel, depending on the Mg/Ca peak intensity ratio, only the property called “phase” was changed, without changing the original crystal orientation. Before continuing with the data processing, tests were made that the above operation did not introduce errors in the crystal orientations (compare Fig. S1c and Fig. S1h).

Dolomite is commonly characterized by systematic misindexing of 180° around the a-axis direction (i.e., $\langle 11\bar{2}0 \rangle$; Fig. S2) due to the pseudosymmetrically equivalent patterns that are sufficiently similar and only differ by one or two, often weak, diffraction bands (Pearce et al., 2013). Due to the presence of both calcite and dolomite in our samples, efforts were made during the data cleaning phase to try to overcome the problems arising due to systematic misindexing of dolomite. Although in MTEX it was possible to distinguish grains boundaries characterized by the $\langle 11\bar{2}0 \rangle$ misindexing, removal of the pixel with the wrong orientation was carried out by merging them with the host grain (function *merge* in MTEX). This function recalculates the mean orientation of a grain accounting for pixels that were previously considered as separate grains (i.e., misorientation angle ≥ 10°). This step modifies the original orientation of the host grain by a magnitude directly proportional to the amount of misindexed pixels in the dolomite grain. Therefore, because of the significant additional error introduced during the correction of the dolomite systematic misindexing, dolomite orientation data were plotted without the merging between the misindexed pixel and the host grains. As a consequence, the dolomite orientation data could still be interpreted, taking into account the non-reliability of the polarity of the c-axis, but the reliability of its orientation (non-polar).

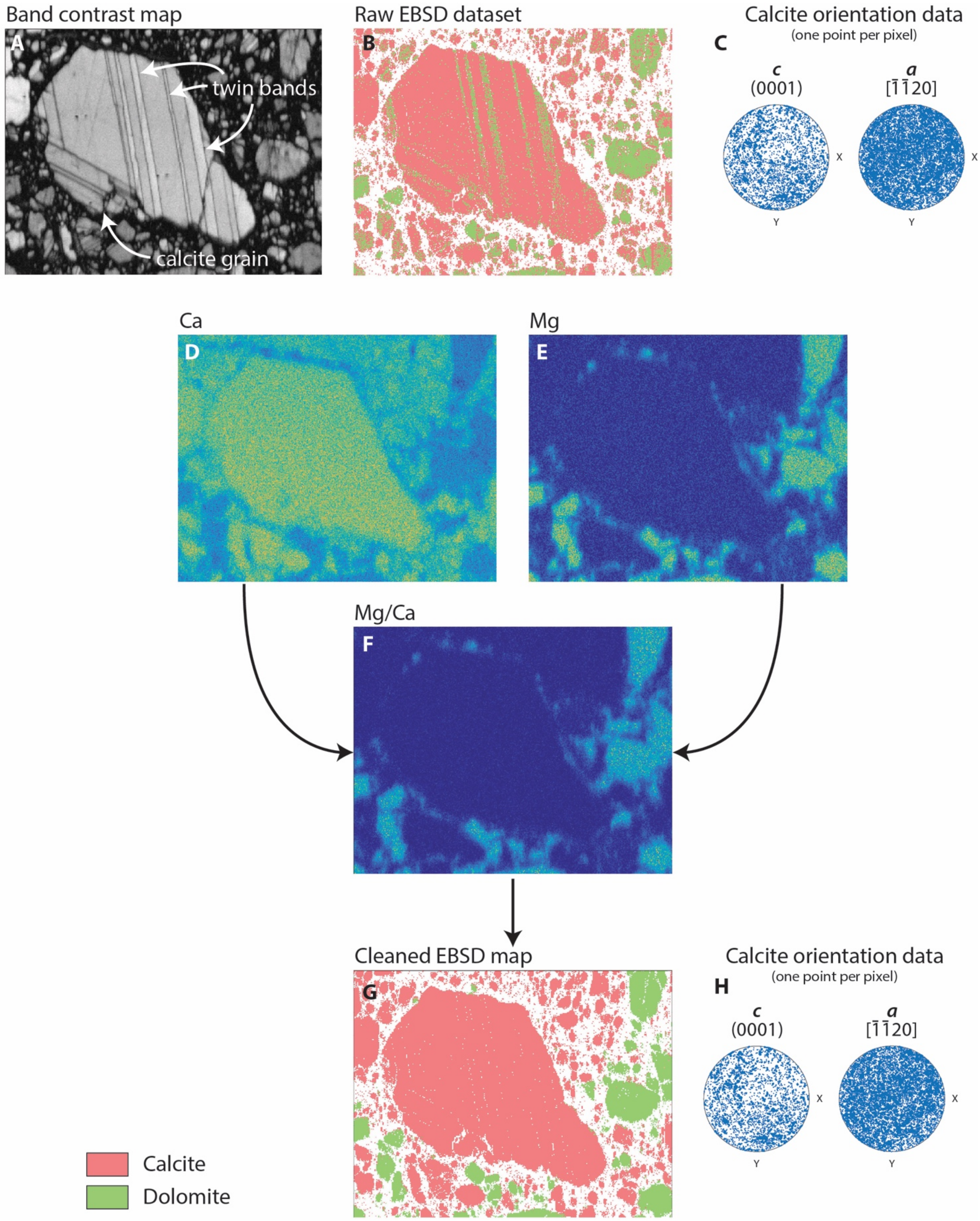

Fig. S1. Workflow to postprocess EBSD data. a) Detail of a band contrast map from sample s1217. b) Phase map of the raw EBSD dataset showing typical misindexing between calcite and dolomite. In this case, misindexing mainly occurred along the twin bands in the calcite grain and at the border of dolomite grains. c) Pole figure of orientation data for calcite (one point per pixel) from the raw EBSD dataset shown in part b. d) EDS map for Ca. e) EDS map for Mg. f) Map of the Mg/Ca peak intensity ratio. Dolomite was dentified with a peak intensity ratio ≥ 0.2, while calcite with a peak intensity ratio ≤ 0.15. g) Phase map of the cleaned EBSD dataset. Voids within the grains were filled later in the data processing procedure by controlled grain “growth” in MTEX. h) Pole figure showing orientation data for calcite (one point per pixel) after the "cleaning" procedure. No significant variation in the orientation was detected with respect to the raw dataset.

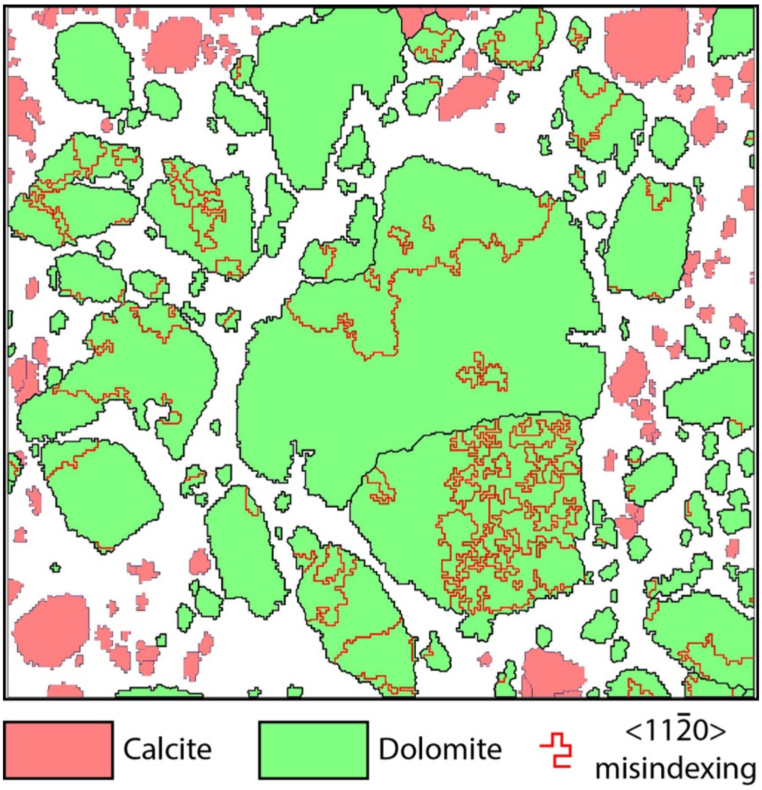

Fig. S2. Systematic misindexing occurring in dolomite grains. Dolomite is characterized by systematic misindexing of 180° around $\langle 11\bar{2}0 \rangle$. Black lines define grain boundaries in dolomite while red lines represent misorientations corresponding to misindexing on the a-axis.

2. Eigenvalue analysis

The clustering strength was quantified using the eigenvalues orientation tensor (Woodcock, 1977). Eigenvalues S_1, S_2 and S_3 (where $S_1 > S_2 > S_3$) are related to the shape and the strength of the distribution of a specific crystallographic direction. Here, we calculate the eigenvalues for the (0001) and use the normalized form, so that $S_1 + S_2 + S_3 = 1$. In a log-log diagram, where the x-axis is $\ln(S_2/S_3)$ and the y-axis is $\ln(S_1/S_2)$, CPOs characterized by $S_1 > S_2 \approx S_3$ are clusters, and CPOs with $S_1 \approx S_2 > S_3$ are girdles (see Fig. 1 in Woodcock, 1977). The strength of the c-axis (in this case) alignment is given by the parameter:

$$\boldsymbol{C} = \ln(S_1/S_3) \qquad \text{(Eq. 1)}$$

which ranges from 0 to infinite.

Eigenvalue analysis of the c-axis distribution resulted in most of the data plotting on the left side of the girdle/cluster transition in the two-axis logarithmic plot (Fig. S3a), suggesting a cluster distribution for the calcite c-axes. In the uniaxial stress experiment, no CPO was observed with ***C*** being 0.44 (dashed line in Fig. S3b). The sheared gouges from three water-dampened experiments had ***C*** values for calcite similar to the uniaxial stress experiment (0.37-0.53), while one sample (*s1213*) showed higher values (0.9). All gouges sheared under room-humidity conditions had relatively higher ***C*** values for calcite, commonly > 1 and up to c. 1.5. The pure calcite gouges also showed a relatively high ***C*** value (Fig. S3b). In the pure dolomite experiments the CPO was weaker, with a ***C*** value similar to the range of water-dampened experiments (Fig. S3b).

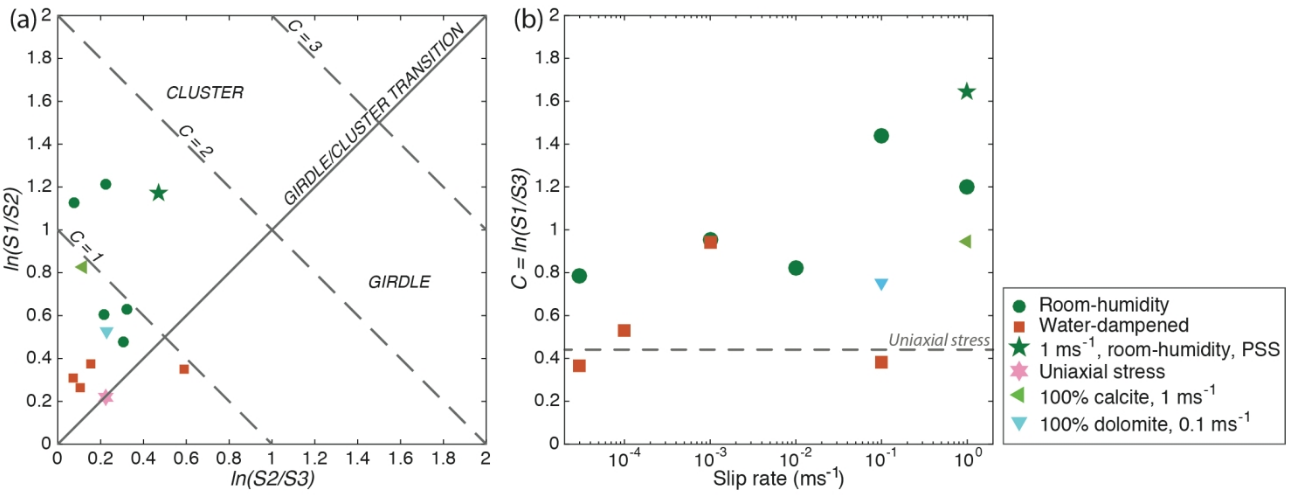

Fig. S3. Eigenvalues analysis. a) Two-axis logarithmic plot of ratios of normalized eigenvalues of (0001) S1, S2 and S3, following the method outlined in Woodcock (1977). b) Plot of ***C*** vs. slip rate. The uniaxial stress case is indicated with a gray dashed line.

3. Calcite grain contribution to the CPO

The identification of calcite grains contributing to the observed CPO was achieved by isolating grains whose c-axis orientation is within a 30° cone of the mode of the CPO (yellow star in Figs. S4a-b). Only non-twinned grains were considered to eliminate the potential bias introduced by considering each twin band as a separate grain. The resulting map (Fig. S4b) shows that the CPO defined by clustering of the c-axes is made up of grains ranging from c. 4 - 70 μm in size that are quite evenly distributed throughout the analysis area, and that such grains compose c. 7% of the entire population of calcite grains.

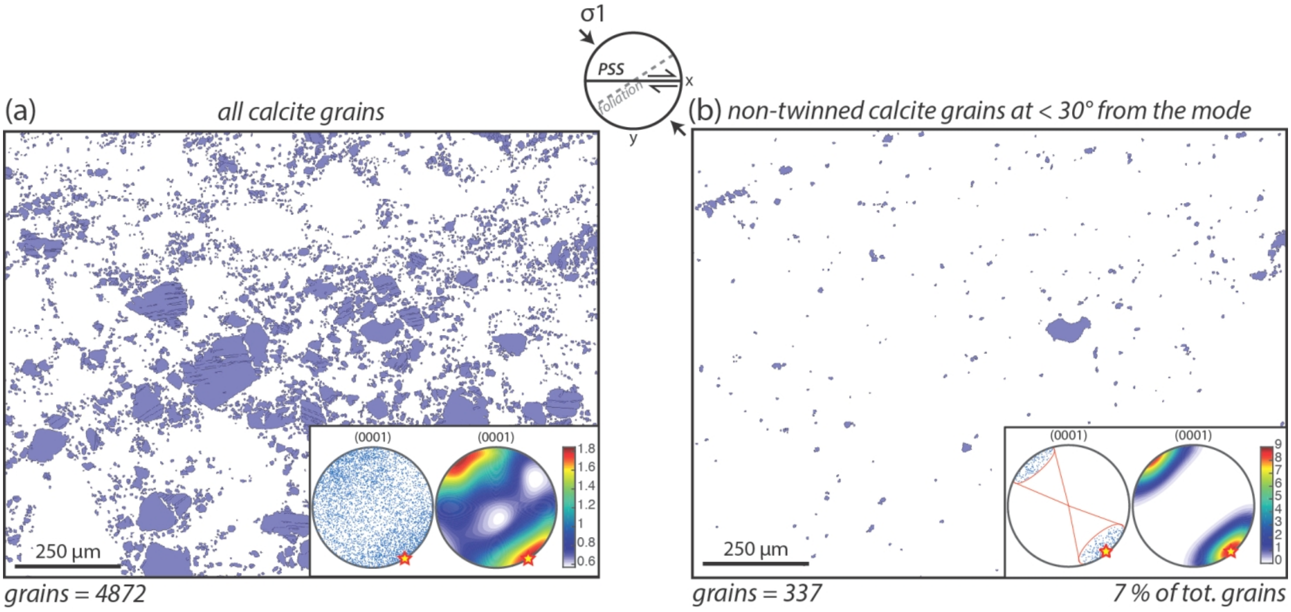

Fig. S4. Contribution of calcite grains to the CPO. a) Map highlighting the distribution of all calcite grains. Pole figures show the development of a CPO with the c-axes oriented sub-parallel to σ1. b) Map highlighting the distribution of non-twinned calcite grains with c-axes lying within a 30° cone of the mode of the CPO (yellow star on pole figures).

4. Calcite intragranular low-angle misorientation boundaries

As shown by the misorientation angle distribution analysis in Fig. 6b-d in the main text, the calcite misorientation angle distribution shows an increase in low-angle boundaries and a clear peak around 77° for the neighbor-pair grains distribution.

Maps of grain boundary misorientation angles in calcite show that low-angle boundaries (with misorientation angles < 10°) occur close to fractures, or correspond to the fracture traces themselves. The low-angle boundaries are likely formed by small displacements and rotations across the newly formed fractures (Fig. S5). There are no low-angle boundaries that occur within largely intact portions of calcite grains suggesting the activity of subgrain rotation recrystallization.

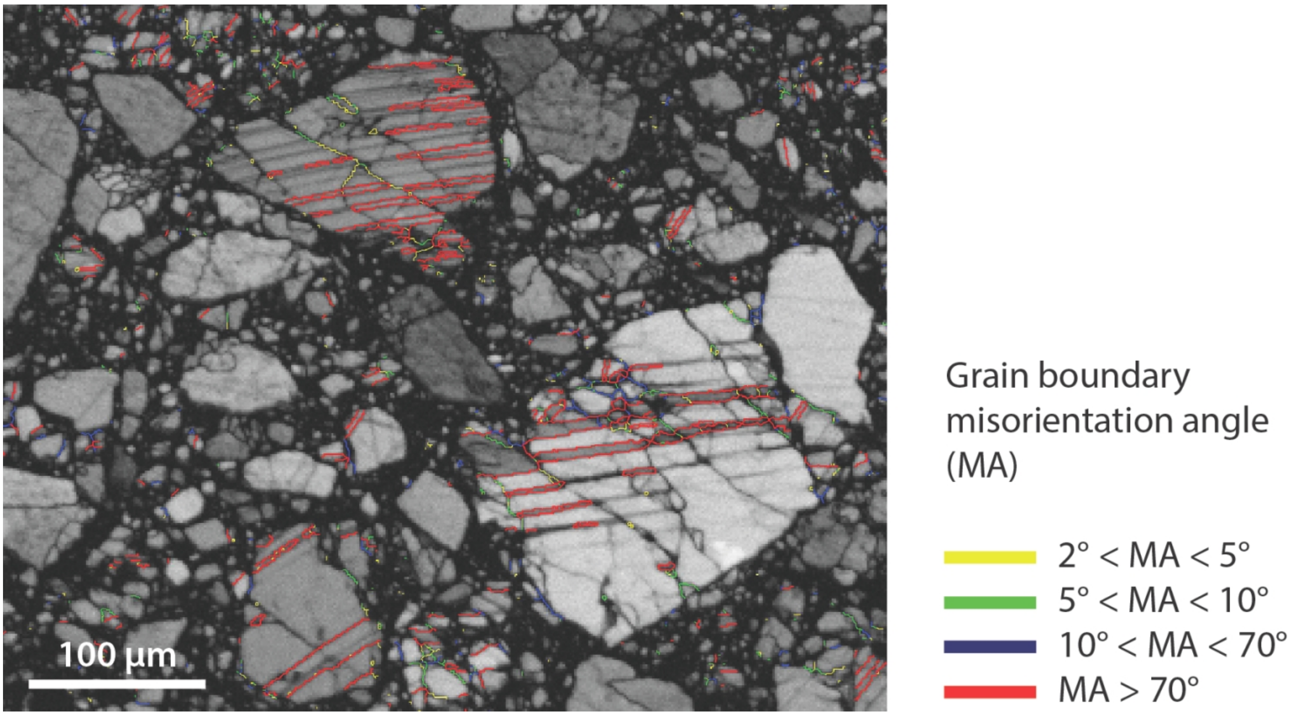

Fig. S5. Intragranular low-angle misorientation boundaries in calcite grains.

References

Woodcock, N.H., 1977. Specification of fabric shapes using an eigenvalue method. Bull. Geol. Soc. Am. 88, 1231–1236. doi:10.1130/0016-7606(1977)88<1231:SOFSUA>2.0.CO;2.